2018-05-22

Frost Heave as the Main Process Defining Natural Unforested Areas below a Temperature Treeline

Toloui-Semnani, Moujan

UNIVERSITY OF CALGARY

Frost Heave as the Main Process Defining Natural Unforested Areas below a Temperature Treeline

by

Moujan Toloui-Semnani

A THESIS

SUBMITTED TO THE FACULTY OF GRADUATE STUDIES

IN PARTIAL FULFILMENT OF THE REQUIREMENTS FOR THE

DEGREE OF MASTER OF SCIENCE

GRADUATE PROGRAM IN BIOLOGICAL SCIENCES

CALGARY, ALBERTA

MAY, 2018

ABSTRACT

Jumping Pound is a treeless ridge, with a SE-NW strike of faults and thrust sheets in the Foothills of the Canadian Rockies, stretched more or less perpendicular to the direction of the winter wind that transports the snow off the ridge. This thesis examines the occurrence of frost-heave as well as the yearly frost-heave temporal window in Jumping Pound ridge. Seeds from the trees in the forested adjacent SW slope are dispersed at the end of fall and travel primarily toward the direction of the dominant wind into the ridge crest where they overwinter. This thesis demonstrates that in the growing season, there is sufficient regolith moisture for germination. However, in the following fall and winter the seedlings are uprooted due to constant regolith movement. The snowless, cold soil surface temperatures create a steep gradient of temperature at lower depths, driving the process of frost-heave. The driving mechanisms for the frost heave in this region are identified and analyzed.

Acknowledgements

I would like to thank my supervisor, Dr. Edward A. Johnson. This project would not have been possible without his immense support and patience. My beloved brother, Borzumehr Toloui-Semnani who helped and guided me in every step of this journey. My daughter Anousha Semnani, and my parents Mehranoush and Farrokh Toloui-Semnani. Their love and belief in me has always been a pillar in my life. My Fiancé, Ebrahim Salehi whose support and encouragement spurred me through the most difficult times.

I would also like to thank my current and former lab mates who helped me with data analysis and advice: Patrick Jablkowski, Atoossa Bakhshaii, and Junyan Ding. My field and laboratory assistants: Sarah Kroeker and Matt McLeon. This research was supported by Natural Sciences and Engineering Research Council of Canada.

Table of Contents

List of Tables

List of Figures and Illustrations

INTRODUCTION

Much attention has been directed at the temperature treeline, both in terms of the cause of its position and its movement in the past and particularly its position in the future under a warming climate (Korner 1998; Körner & Paulsen 2004; Harsch *et al.* 2009; Korner and Riedl 2012; Pecher, Tasser & Tappeiner 2011). When the average temperature of the growing season is lower than approximately 5.5-7.5□C, trees are not able to establish and grow due to physiological constraints (Korner 1998). This is known as temperature treeline or treelimit as the resriction is due primarly to temperature. The elevation of temperature treelines in the Foothills of the Canadian Rockies is around 2400 m, this elevation lowers at higher latitudes (Gadd 2008). However, below the temperature treeline, there are areas without forests that are the result of several natural causes. Temporary natural unforested areas are result of snow avalanches, wildfire and insect outbreaks, and other natural forest disturbances (Collins, Everett & Stephens 2011; Johnson and Miyanishi 2010; Woods 2004; Shatford 2007). Long term natural unforestation results from landslides, block fields, and talus slopes (Oelfke & Butler 1985; Malanson *et al.* 2002; Leonelli *et al.* 2016). Also, there are areas unforested because of distinctive lithology and soil, which have high concentrations of chemicals that limit vegetation e.g. serpentine rock and soil (Kruckeberg 2002, Shaw et al. 1989). Further, there are areas which have microclimates that prevent or severely limit trees (Plasse & Payette 2015) by creating frost hollows during the growing season. Finally, trees require a cohesive regolith, sufficient rooting depth and regolith which is not moving. This movement can be due to several causes, landslides, debris flows, rock creep, talus creep, soil creep, solifluction and frost heave.

Here we will study an unforested ridge crest at approximately 2200 meters with no evidence of past trees (Figure 1). This unforested ridge is below the regional average treeline and other ridges nearby at the same elevation are treed. This ridge is also not unforested due to any aformentioned naturally short or long term causes.

The ridge is part of a thrusts-fold system associated with the Dyson Mountain fault. The Dyson Mountain fault is immediately to the east of the McConnell fault (the boundary between the Front Range and Foothills of the Canadian Rockies). The ridge's regolith is more than one meter deep and made up of weathered shale, siltstone, and sandstone, black in color with high organic content. The substrate is not considerably different from the immediate adjacent slopes which are forested with Lodgepole pine *(Pinus contorta Loudon*), Engelmann spruce (*Picea Engelmannii* Parry *ex* Engelm.) and Subalpine fir (*Abies lasiocarpa* (Hook) Nutt.). The ridge is generally blown free of snow during large parts of the winter. Stone stripes (French 1996) are present on the ridge. The rige is covered with herbaceous and woody plants that have root systems suggesting movement of the substrate as on scree slopes e.g. Pérez (1998).

Here we will examine the processes that contribute to the lack of trees. We will start by investigating the question of weather the regolith water content on the ridge is adequate during the growing season for tree growth. To answer this question we hypothesize that trees do not establish on the ridge crest because of the seasonal precipitation distribution and the regolith water potential. The second question we examine is weather young tree seedlings are uprooted by regolith frost heaving during winter. Here we hypothesize that trees do not establish on the ridge crest because of the structural geology, lithology, regolith temperature gradient, and wind that blows snow off the ridge during the winter. All these factors work through the processes of frost heave.

Our results show the importance of the interaction of physical processes in creating a zone from the bedrock to regolith (both saprolite and entisols) to the boundary layer that create the conditions that trees cannot survive and grow.

RESEARCH SITE DESCRIPTION

The study was conducted on Jumping Pound Ridge, located in the Foothills of the Canadian Rocky Mountains in Kananaskis Country, Alberta, Canada (elevation ~2200 m, lat. 51.087, long. -116.061 or UTM Zone 11U 565765 Easting, 5659919 Northing (Figure 1)). The Foothills consist of a series of thrust faults of sedimentary rocks (Osborn, Stockmal & Haspel 2006;). The Jumping Pound Ridge (thrust) is comprised of several formations (from low elevation to high): Mesozoic Fernie Formation (JF) shale with minor sandstone; Kootenay Group (JKK) sandstone, siltstone, some mudstone, conglomerate, and coal; Blairmore Group (KBL) fossiliferous shale, sandstone, conglomerate; topped by Blackstone Formation (KBK) shale, sandstone, and siltstone. There is no sign of glaciation as till, outwash, or erratics.

The climate is transitional Plains-Cordilleran with Foothills climate characteristically having warm summer with higher precipitation in late May and early June and cold winters and higher precipitation in summer than winter (Charron & Johnson 2006). The annual precipitation is 347 mm with 284 mm from rainfall and 63 mm from snowfall (Barrier Lake Station, AB, Latitude: 51.1° Longitude: -115.1° Altitude: -9999 m).

The study area (Figure 2) is divided into a steep north-facing aspect forested by Engelmann spruce, Subalpine fir and some Lodgepole pine, a gentle south-facing aspect that is forested by spruce and pine and the ridge crest meadow covered with *Dryas octopetala L.*, *Saxifraga* *bronchialis L.,* and *Sedum integrifolia (Raf.) Love &Love*.

The three instrumented sites are: Site 1 represents the unforested ridge (meadow) (Elevation: 2200 m), Site 2 (Elevation: 2191 m), and Site 3 (Elevation: 2182), are the forested area on the steep NE-facing slope and gentle SW-facing slope respectably. Sites 2 and 3 were used to compare processes of the forested landscape to the unforested ridgeline.

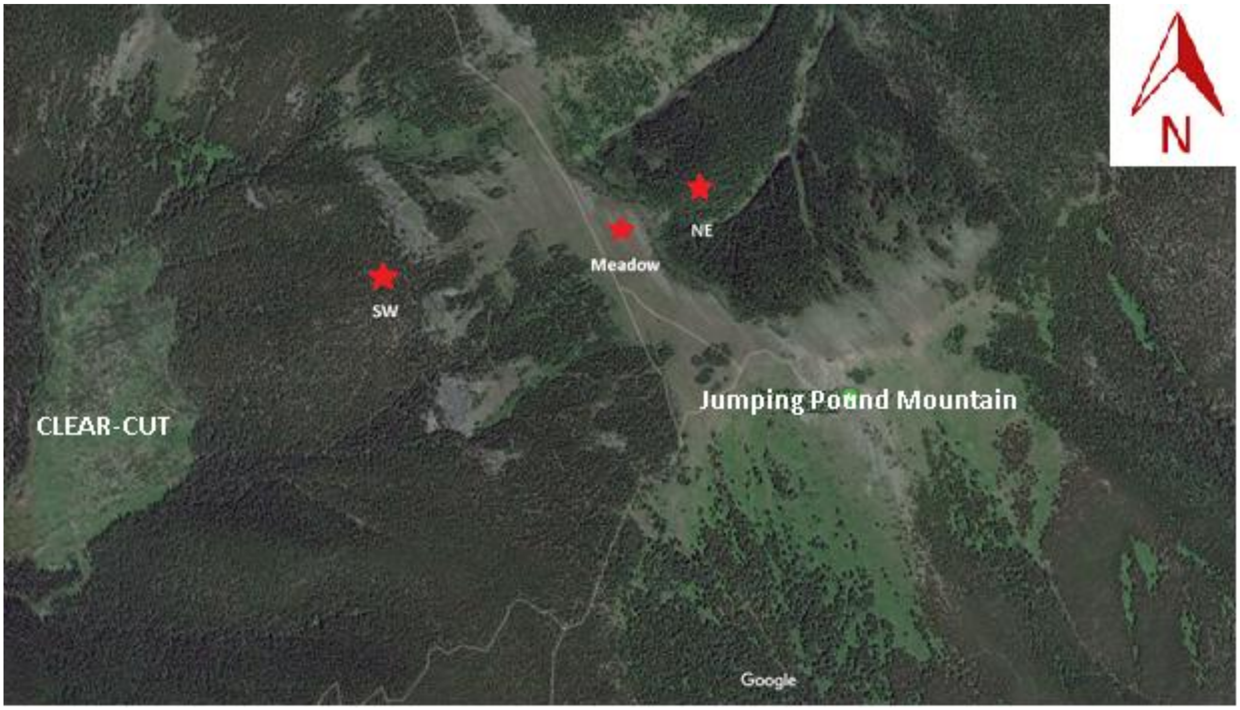

Figure 1. Google image of Jumping Pound Mountain 2018. Showing the instrumented sites and the location of the clear-cut at the left edge of the image. The lines represent footpaths.

Figure 2. Jumping Pound Ridge top left: July 2015, top right: September 2015, bottom left: November 30 2016 & bottom right: January 30 2016, looking north.

METHOD

Instrumentation (Table 6S, Appendix 1)

Each instrumented site consisted of matric moisture (Delta-T theta capacitance probes) and temperature probes (HOBO) installed at 10, 20, 30 and 40 cm depth recording hourly. Soil heat flux was measured using two soil heat flux plates model HFP01 (Campbell Scientific) placed at the depth of 8 cm. Surface and atmospheric conditions were monitored with a net radiometer (Kipp and Zonen NR-Lite), infrared surface temperature sensor, wind speed sensor (HOBO), air temperature and pressure sensors (HOBO). The heat flux plates, net radiometer, wind sensor, temperature and relative humidity sensors took four-hour averages of samples read every four minutes. All measurements were then averaged over 24-hour periods. Precipitation was measured using tipping-bucket rain gauges (Onset instruments). Matric water potential was measured directly on the unforested ridge using three tensiometers model SK20 (UMS). Regolith samples for calibration of matric moisture sensors and regolith texture characteristics were taken within two meters from the instrument sites. Samples were air dried in the lab and sieved to <2 mm. The particles were dissolved of organics with Hydrogen Peroxide and were separated with a 5% Calgon solution before running them through the particle analyzer (Malvern Mastersizer 200). Saturated conductivity was measured using a 14.75 cm radius metal infiltration ring. The ring was pushed into the ground to a depth of 6 cm. Six locations were selected for the meadow both in stone-stripe and vegetation areas. Three locations each for the forested SW and NE sites were selected based on vegetation canopy. Initial soil moisture was taken at all locations in the ring before four liters of water was poured into the ring. End-time was taken once all pooled water within the ring had been absorbed into the ground. Then the final soil moisture was taken at all locations in the ring. The saturated hydraulic conductivity was measured using the (Wooding 1968) equation:

$$K_s = \frac{is}{\frac{1+4\lambda}{\pi r}} \qquad \textbf{1)}$$

where K_s is the saturated hydraulic conductivity, *is* is the steady infiltration rate, *r* is the radius of the ring and λ is the macroscopic capillary length chosen from (Elrick & Reynolds 1992) based on soil texture structure categories.

Water Availability and Evaporation

The matric water potential gives the availability of water in the regolith for plant uptake. The Van Genuchten (1980) equation was used to fit the soil-water content to the water potential from pressure plate extraction of regolith samples collected at the study sites. The matric potential is given by the Van Genuchten equation, where n, m and α are fitting parameters, θ_r is the residual water content, θ_s is the saturated water content, and θ_{effp} is the effective volumetric water content ($cm^3\ cm^{-3}$):

$$\psi_{\mathrm{ave}_p} = \frac{\sqrt[n]{\frac{1}{\sqrt[m]{\theta_{\mathrm{eff}_p}}} - 1}}{\alpha} \qquad \textbf{2)}$$

$$\theta_{\mathrm{eff}_p} = \frac{\theta_{\mathrm{ave}_p} - \theta_r}{\theta_s - \theta_r} \qquad \textbf{3)}$$

The field-measured saturated-hydraulic-conductivity (explained above) was used, and α and n were chosen based on pedotransfer functions (Schaap, Leij and Van Gencuhten 2002) derived from the proportions of sand, silt and clay in each site. Parameters were chosen to maximize model fit to measured soil moisture content.

Potential evaporation was calculated using the Shuttleworth (2007) modified and adapted Penman equation:

$$E_{\text{mass}} = \frac{mR + \gamma * 6.43(1 + 0.536 * U)\delta e}{\lambda\nu(m + \gamma)} \qquad \textbf{4)}$$

where E_{mass} is the evaporation rate (mm day^{-1}), m is the slope of the saturation vapour pressure curve (kPa K^{-1}), R is the net radiation (MJ m^{-2} day^{-1}), γ is the psychrometric constant = (0.0016286 * P_{kPa})/ λ_v (kPa K^{-1}), U is the wind speed (m s^{-1}), δe is the vapor pressure deficit (kPa), and λ_v is the latent heat of vaporization (MJ kg^{-1}). This equation implicitly includes the division of the numerator by the density of water (1000 kg m^{-3}) to obtain evaporation in units of mm d^{-1}.

Seed Planting Experiment

From the 20 to the 30 of July 2015, seeds of the three native tree species (*Abies lasiocarpa, Picea Engelmannii and Pinus contorta*) were germinated in the laboratory and, then along with un-germinated seeds, were both planted and sown at the ridge (meadow) site in three different locations. The location of the plots was chosen so that they would cover the entire width of the meadow from the higher NE side to the mid-level and the lower SW side. Each location had nine plots, three plots for each species. In one plot, the seedlings were planted directly onto the surface. The second plot had seedlings that were individually planted into the soil and partially covered. In the last plot, the seeds were scattered along the surface of the plot. All plots were saturated with water after planting. In May 2016, each plot was examined for survivors.

Empirical measurements of the surface regolith movement

In August 2015, 15 stone stripes were chosen using the grid and random number generator method. Soil samples were collected and analyzed from the 15 stone stripes and compared to the soil sample compositions taken from vegetative areas in proximity of the instrumentation. The decision was made to only use stone stripes for frost-heave movement measurement, as the soil composition of the first 10 cm of the vegetative areas and the stone stripes were comparable (Table 1 and 2). In addition, on the surface of the stone stripes gravel was present that could be used to observe and measure movement. Using a permanent red spray paint, 20 cm x 20 cm squares were painted on all 15 chosen stone stripes and photographed (Figure 3).

In July of 2016 pictures were retaken and all the stones were flipped over to see if the underside was painted (Figure 3). In addition, the thickness of the fine debris layer (regolith < 2 mm in diameter that is relatively loose and can move easily) of the first 15 cm of soil was measured by digging pits adjacent to the painted squares. The slope of each square was measured using a Brunton compass. All the individual stones collected were counted in the lab, weighed and the largest side measured. The first and second-year photos were compiled and the photos of the same squares from different years were compared with each other.

Making the bottom left hand corner of the painted section the relative point of origin (0, 0) in each photo, a floating ruler was used to take the horizontal and vertical point of stones at each location in both year 1 and year 2 photos. The difference between the horizontal and vertical coordinates of each year for each stone was taken. The Pythagoras Theorem was then used on the difference between the horizontal and vertical coordinates of each year, and for each stone, to get the difference in location of the stone. This value was adopted as the measure of regolith velocity per year:

$$(x, y)_{2015} - (x, y)_{2016} = (x, y)_{\text{diff}}$$

$$D = \sqrt{x^2 + y^2}; \quad D = \text{distance travelled} \qquad \textbf{5)}$$

Empirical Frost-Heave Calculations

Annual regolith velocity V_s was calculated using (Matsuoka 1998) and compared to the field measured value:

$$V_S = C_4 DSCN \tan^2 \theta \qquad \textbf{6)}$$

where C_4 is a dimensionless coefficient, D is the fine debris thickness within the top 15 cm of the regolith, SC is the ratio of soil finer than 0.063 mm (silt and clay content of the soil), N is the effective number of frost-heaves per year calculated based on the melting and freezing temperature of ice and water within the specific soil composition and θ is the slope. When the spatial variation in soil moisture and net radiation is small the diurnal frost heaving is a function of the thickness of the near-surface fine debris layer and its silt and clay content since the pore size in regolith affects the suction force and therefore the amount of heave (Everett 1961;

Matsuoka 1998). Placing the cycles rate (N in Equation 6) and the values from Table 4 into Equation 6 gives the result in centimeters per year.

Figure 3. Painted squares number 3 on the Meadow of Jumping Pound Ridge, photographed August of 2015 (left photo) and July 2016 (right photo).

Processes model for Frost-Heaving

At temperatures lower than but approaching the bulk melting temperature (T_m~0°C), water exists both as liquid and as ice. At these temperatures a thin layer of fluid remains as a pre-melted film between soil grains and ice (Rempel, Wettlaufer & Worster 2001; Dash, Rempel & Wettlaufer 2006; Wettlaufer & Worster 2006) Water tends to moves toward colder temperatures and supplies the growing ice-lens inside the pores of fine-grained soil. The build-up of ice produces the measured frost-heaving in the regolith (Nixon 1991; Rempel *et al.* 2001; Press 2017) where the ground surface is being displaced vertically upward.

The frost heave regime has three regions in the regolith with depth: an ice lens on the upper part, a frozen fringe that forms the level below in which water and ice coexist between the pores in the midst of regolith particles, and finally, the warmer level below where water fills the pore without any ice formation. However, the middle layer, the frozen fringe, does not necessarily exist in every region, and where it does not exist, frost heave cannot take place. The amount of liquid water that is held between soil grains at temperatures (T) lower than the bulk melting temperature T_m is strongly dependent on regolith size. Frost-heave susceptible soils such as silt will have pore spaces that are small enough for water to be held with capillary forces above the water table but also large enough to contribute to the growing ice lens (Rempel 2010).

The methods of Nixon 1991; Rempel 2004, 2007, 2012; Rempel, Marshall & Roering 2016, were used to model the occurrence and to predict the possible temporal window of frost-heaving at the meadow sites.

Our model is one-dimensional and parametrized by a single variable z denoting the depth level. The depth is measured from the level where the temperature is equal to freezing temperature of water T_m. The value of T_m depends both on the geographical coordinate of the region as well as its depth level and is therefore usually not equal to zero degrees Celsius but close (typically~ -0.1°). Thus, one boundary condition of our model consists of an isotherm at $T = T_m$ that corresponds to z=0.

The frozen fringe, begins at depth level $z = z_F$ and the ice- lens at (the higher) level which we denote by $z=z_L$. The second boundary condition consists of boundaries in the interface between ice and water in the pores of soil particles within the frozen fringe and ending at the level of the ice lens at z_L constituting a complex network of total surface area Γ. In other words, denotes the total surface of the ice that is connected to the ice-lens. In our model, we consider the direction associated with every infinitesimal section d_i to be pointing in the direction of the outward normal to the ice. To form a closed region (for later integration purposes) we include the surface of the isotherm region at level $z = z_L$ of area A to the total area Γ. In our one-dimensional model, we take the cross section of this interface area as the other boundary condition.

This boundary at $z = z_L$ in general can move and change relative to the frame that is fixed at z = 0. All the calculations in our model are relative to this fixed frame unless otherwise stated.

Next, we determine the rate at which this boundary changes position. Let the temperature at the ice-lens $z = z_L$ be denoted by T_L, and at the beginning of the frozen fringe (assuming it exists) as T_F. The temperature in the model between T_m (z = 0) up to T_L at the depth of the ice-lens has a constant gradient ∇T that plays an important role in determining the emerging characteristics in our model. In the presence of frost heave, saturated soil underneath the depth z=0 is pulled through the range of our model (from z=0 to $z=z_L$ due to this temperature gradient at a constant speed V in the coordinate frame fixed at the z = 0 isotherm cross section pushing the ice lens upward and causing the ground level to heave and eventually fall over.

This constant speed is referred to as the freezing rate. The pulling thus causes a movement of the ice lens relative to the soil particles at the velocity V_L, namely the heave rate. The rate of change is

$$\frac{dz_L}{dt} = V = V_L(t) \qquad \textbf{7)}$$

In other words, the boundary remains stationary relative to the lower isotherm boundary z = 0 if $V = V_L$. It moves away from the lower isotherm boundary up to the frozen region if $V > V_L$.

Two necessary conditions are required for frost-heaving to take place. First condition, places a constraint on the characteristics that a soil must possess in order to be susceptible to significant heave (Rempel, Wettlaufer & Worster 2004)

$$R_p \leq \frac{4\phi\gamma_{s\ell}}{P_0} \qquad \textbf{8)}$$

where R_p is the characteristic radius of the 'throats' between pores (i.e. pore throats), φ is the porosity in the soil (constant), γ_{sl} is the surface energy of the solid-liquid interface and P_0 is the downward pressure from the top layers of the ice lens (overburden pressure).

The second condition requires that the right-hand side of Equation 9 which is a function of temperature gradient and the fraction of pore volume filled with ice in the frozen fringe (S_s) be greater than downward pressure from the top layers of the ice lens (P_0).

$$P_0 < P_{\max} = \rho G z_L - \rho G \phi \int_0^{z_L} S_s(z)dz = \rho G \int_0^{z_L} (1 - \phi S_s(z)dz). \qquad \textbf{9)}$$

where $P_{max} = P_T + P_\mu$ and P_T is the upward pressure due to the intermolecular forces and P_μ is the downward hydrodynamic pressure due to water moving up to supply the ice-lens. ρ is the density of water, z_L is the vertical distance where ice-lens forms; where

$$G = \frac{L}{T_m}|\nabla T| \qquad \textbf{10)}$$

L is the latent heat of fusion, T_m is the bulk melting temperature, ∇T is the constant temperature gradient with in soil layer where

$$\nabla T = \frac{T - T_m}{z} = \frac{T_L - T_m}{z_L} = \frac{T_F - T_m}{z_F} \qquad \textbf{11)}$$

and T_L is the temperature at the point where ice-lens forms; T_f is the temperature at the point where the frozen fringe forms; z_f is the vertical distance where frozen fringe begins (Figure 4). To estimate the parameter S_s, we used the following relation:

$$1 - S_s(z) = \frac{A(-T(z))^B}{w_{\text{tot}}} \qquad \textbf{12)}$$

where A and B are constants table 1 in (Nixon 1991) based on the soil type and w_{tot} is the total gravimetric water content.

This model is applied only to the days that the soil at different depths reach their undercooling $\Delta T = T_m - T$. The threshold undercooling for ice formation in pores is controlled by curvature effects:

$$\Delta T_F = \frac{2\gamma T_m}{\rho L R_p} \qquad \textbf{13)}$$

where ΔT_f is the undercooling at which ice first appears in the pore space ($\Delta T_f = T_m - T_f$ where $\Delta T \geq \Delta T_f$) $\gamma \approx 0.035$ J/m^2 is the ice–liquid surface energy, Rp is a characteristic pore dimension, and the coefficient $2\gamma Tm/(\rho L) \approx 0.06$ ◦Cμm. (Rempel, Marshall & Roering 2016).

With the assumption that the pore sizes at different depths are of the same order as the measured size of the soil, the deduction was made that the maximum water/ice temperature below which undercooling takes place is:

T_m – 0.06°C/average pore size (μm) = T_f

The difference between the meadows daily soil temperature at different depths and the T_f estimated for the soil size at that level was calculated. This information was used to identify the days when the undercooling took place and the ice-water interfaces were formed for each depth. Next, we made the assumption that the days for which T is less or equal to T_f at the given depth are the days when a force due to undercooling is exerted on the water/ice in the pores, which indicates the existence of frost-heave (Rempel 2012). High soil temperatures means that soil is not able to reach its undercooling, hence leading to no frost-heaving process.

The ground surface at the meadow site is not covered with snow most of the year for more than a short period. During the colder parts of the year, the temperature at the ground level is markedly below the freezing point of water and increases with depth.

In days when the temperature at ground is below the freezing point of water and monotonically increases with depth under the ground, we extend the data comprising the temperature profile by interpolating the temperature values between the four discrete data points and extrapolating the temperature function from the surface to depth z=0 where temperature reaches $T=T_m$, the freezing/melting temperature of water. The interpolation of the data points for temperature are calculated via the **interp1** function in Matlab using the Piecewise Cubic Hermite Interpolating Polynomial (PCHIP) method. The PCHIP method uses both the value of the data points and estimated derivatives at the data points to return a shape-preserving piecewise polynomial structure for the intermediate points of the interpolation. We divide the range for which the interpolation is calculated into unit intervals (corresponding to depths of 1 cm each), so that the result of the interpolation is an array of discrete values consisting of the estimated temperatures at intervals of 1 cm. The extrapolation is also achieved by the same PCHIP method with the extra parameter '**extrap**'. Here too the range of the extrapolation is divided into unit intervals, the result being the array containing the estimated temperature values at discrete depths layers of thickness 1 cm each. The output of the Matlab script is the array **T** of estimated temperatures for the depth coordinates of unit separation stored in an array **z.**

At this stage, we estimate the values for the depth at which the ice lens forms, $z=z_L$, and the corresponding temperature $T=T_L$. The estimated value is determined by the point at which the temperature profile, graph's slope from the surface changes, becoming steeper.

Next, we estimate the second important parameter from the temperature profile, viz. the depth at which the frozen fringe is formed $z= z_F$ and its corresponding temperature $T=T_F$. The estimated point corresponds to the second point on the graph of the temperature profile where the slope changes and almost the linear descent of the graph becomes steeper.

By determining the values of z_L and z_F, we are able to check whether the data is consistent with the existence of three layers predicted by our theoretical model, namely the ice lens, the frozen fringe and the unfrozen soil below it. In case the model is validated in its prediction of the three layers, we can move on with the next phase of our model.

The right-hand side of Equation 9 is a function of temperature gradient and the fraction of pore volume filled with ice in the frozen fringe (S_s) has to be greater than downward pressure from the top layers of the ice lens (P_0). The next step consists of our estimating the average temperature gradient in the frozen fringe region and the unfrozen soil layer below it reaching all the way to the source of water at the freezing/melting level $T=T_m$ (Eq. 11), from which the value of the parameter G (Eq. 10) is calculated for each day during the period through which data samples based on measurements were taken.

The other relevant function of the theoretical frost heave model discussed in the method section is the function S_s, the fraction of the pore volume within the frozen fringe region that is filled with ice; we use the calculated temperature profile as the input to Eq. 12.

Finally we calculate the maximum upward pressure P_{max} due to intermolecular forces by integrating the formula in Eq. 9. The numerical calculations required for this section are performed in Matlab. Using for input the array **T** of temperatures (the final output of the interpolation and extrapolation algorithms) as functions of depth z , we first numerically calculate the best estimate for the gradient and the corresponding parameter **G** using Equation 10. Next we calculate an array $\mathbf{S_s}$ containing the values of the fraction of pore volume filled with ice in the frozen fringe (S_s) in Equation 12. The integration in Equation 9 is performed via the trapezoidal numerical integration algorithm in Matlab (the **trapz** Matlab-function) versus the array **z** of coordinates with unit spacing. We thus generate the intermolecular pressure profile for each day within the range of study.

As was discussed earlier, the frost heave model predicts that frost heave occurs only when the upward pressure P_{max} exceeds the downward pressure P_0 coming from the weight of the top layers of the ice lens..

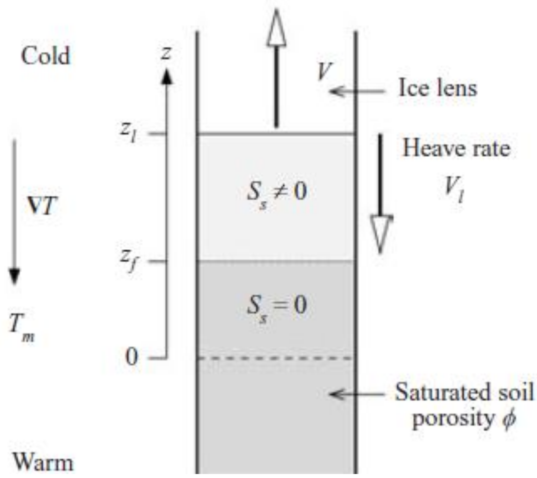

Figure 4. A schematic diagram of an ice lens that is pulled through a temperature gradient at a constant speed or freezing rate V and experiences heave rate V_1. The porosity φ in the soil is constant and the fraction of the pore volume that is filled with ice S_s decreases monotonically from the lens boundary z_l to zero at z_f (Graph courtesy of Rempel *et al.* 2004).

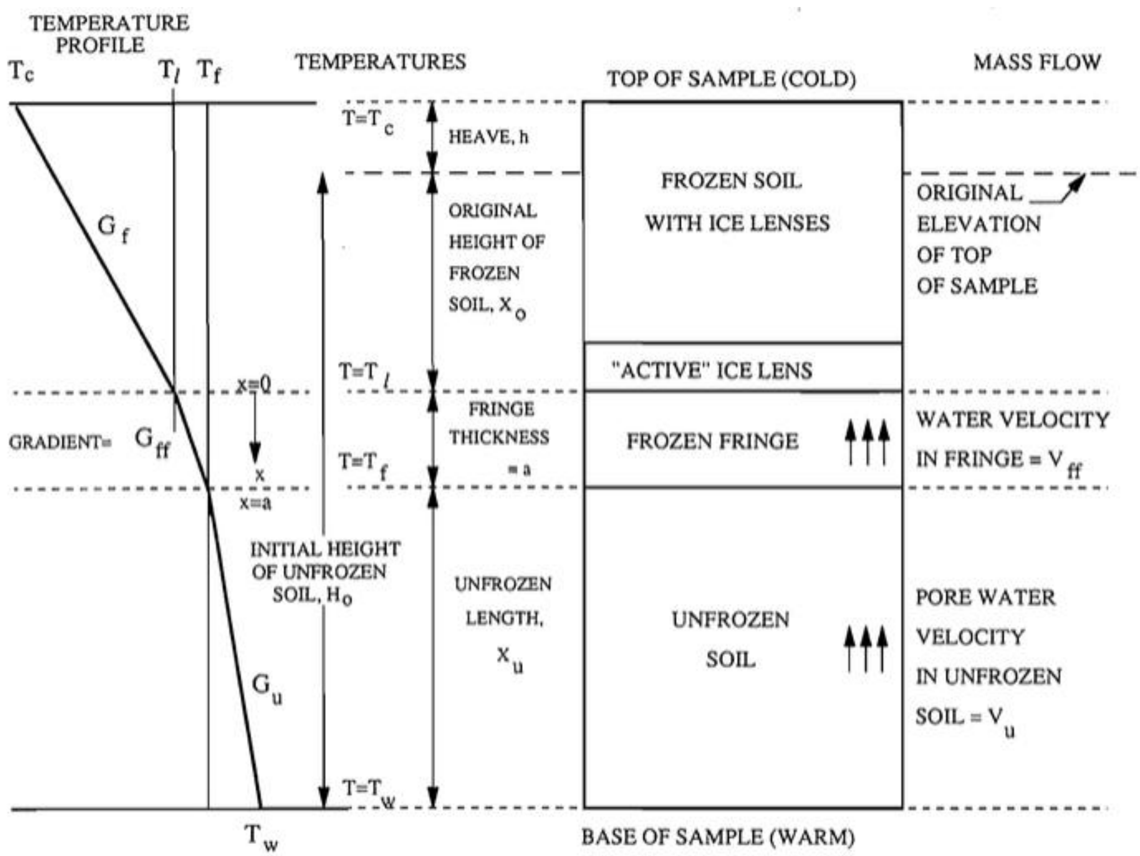

Figure 5. The temperature profile in an idealized 1D soil column in the presence of frost heave. The boundary points z_L (ice lense formation) and z_F (the frozen fringe) can be identified by a change in the slope of temperature versus depth graph (Graph courtesy of Nixon 1991).

RESULTS

Fold orientation and lithology

The treeless meadows (Figure 1) are mostly along the Dyson fault a detachment fold with steep face (~ 45^{O}) (syncline) in the NE displacement direction. The ridge top is dome shaped (anticline) of steep dip up to ~30^{o} to the SW. The Dyson fault encompasses a ridge called Jumping Pound. The fault is the usual old over younger rock with Rundle age (Carboniferous) of limestone emerging at the south end of the ridge. Jumping Pound ridge is part of a bigger structure in which Dyson fault is on the west side of some complex multiple thrust sheets with bent folds (Figure 2) with older Rundle emerging to produce a large limestone structures (Moose Mountain). There is no evidence of glacial material either as till, outwash or erratics. Important in deciding the treeless ridge is the SE-NW strike of the faults and thrust sheets which is more or less perpendicular to the winter wind (Figure 6) that will be seen to be responsible for blowing the snow off during the winter. The dominan wind (Figure 6) blows from west (40% of the time) and south (25% of the time).Also, another important factor is the sandstone and mudstone outcrops on the NE side of the ridge where large amounts of snow are deposited by the winter winds. In the spring this melting snow contributes to the groundwater increase in the meadow.

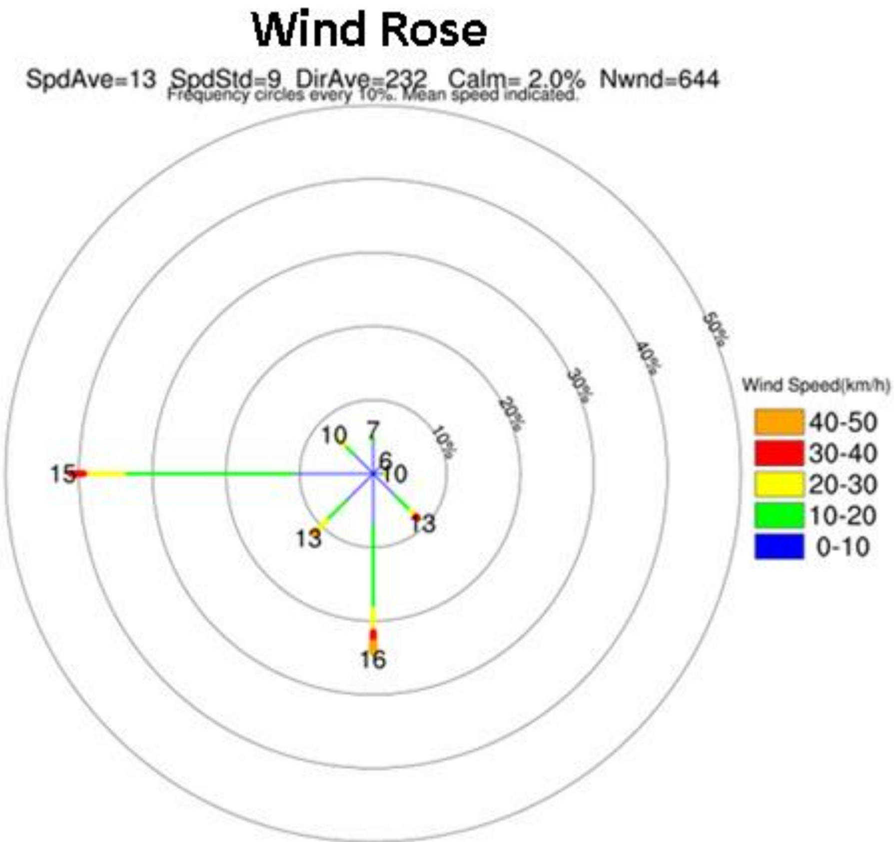

Figure 6. Wind direction (degrees) and wind speed (km/h) in the Meadow from November 2015 to end of March of 2016. The average wind speed is 13 km/h with a standard deviation of 9 and a total of 2% calm days. The average wind direction is 232° (SSW).

Soil Water, precipitation, infiltration, and evaporation

The volumetric water content (Figure 7) of the meadow site and the NE site are similar. The exceptions are short periods of extreme increase in water content in the meadow site associated with snow melt in the NE site and high spring and summer precipitation which results in rise of the water table in the meadow. Notice that water freezes in the surface layer of the meadow during the winter. Also, both the meadow and NE sites have water content 2 to 3 times lower than the SW site. The exception is during peak precipitation on the meadow. All three sites follow the same pattern over the season. The flat periods in winter are when most water is near freezing or frozen. The establishment period of trees is from April to end of August (day of year 92-234). This is the period with the highest regolith moisture content for all sites (Figure 7). Regolith moisture content peaks with snowmelt and precipitation events and drops down in between rain events and after the melted snow drains. Figure 8 shows the flow of water in a first order stream that drains the study area measured using a pressure transducer (Table 6S, Appendix 1). The stream flow is low from September to April when it increases, corresponding to winter snowmelt. The water stays high all summer due to summer precipitation (personal observation).

In winter, the regolith is frozen close to surface in the meadow (Figure 9) which from observation and satellite images is related to little or no snow. The forested sites have more than a meter of snow and soil is generally unfrozen. In May, after the snow melts, the soil moisture content of the meadow peaks as the water table (saturated zone) approaches the surface. In the rest of the summer moisture in the meadow rises only during high precipitation events but then decreases rapidly (Figure 9). The distinctive rapid drop in regolith moisture is due to the high infiltration rate. The meadow (Table 1) has an average infiltration rate of 107 cm/hour which is equivalent to saturated hydraulic conductivity of 62.5 cm/hour or 1500 cm/day. Compared to SW site with an average infiltration rate of 60.5 cm/hour corresponding to saturated hydraulic conductivity of 35 cm/hour or 846 cm/day, and the NE site with an average infiltration rate of 25 cm/hour corresponding to saturated hydraulic conductivity of 14.8 cm/hour or 355 cm/day. All three sites have regolith deeper than one meter and have no soil profile development. The ridge and forested sites all have regolith of weathered shale and sandstone. The meadow and NE have similar proportions of sand, silt, and clay but the ridge has more than twice the gravel content which contributes to its high infiltration rates. The SW site has a much higher clay content (Table 2).

Calculated cumulative evaporation using the modified and adapted Penman Equation (4) (Figure 10) is three times as high in the meadow as in the NE and the SW sites. The evaporation is, in turn, related to the wind speed which is 50 times greater in the meadow compared to the SW site and 10 times greater compared to the NE site (Figure 11 & 12).

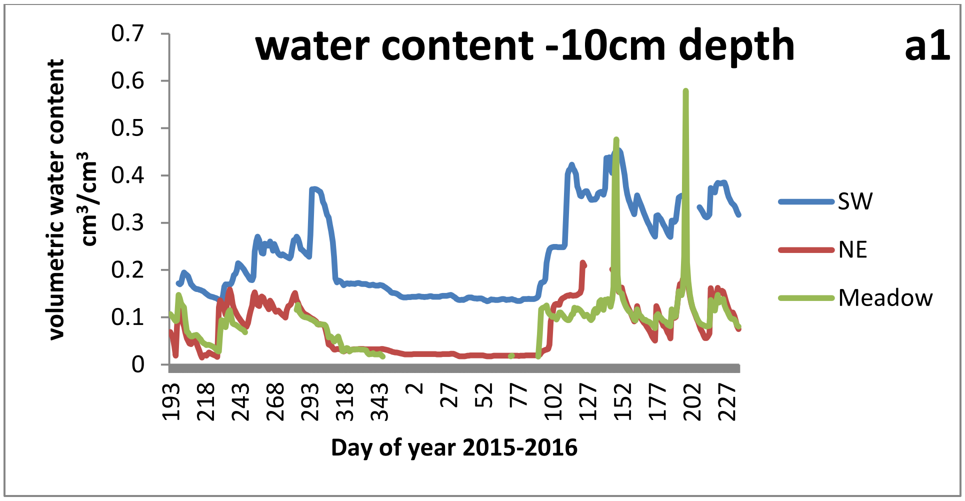
water content -10cm depth
a1
volumetric water content cm³/cm³
0.7
0.6
0.5
0.4
0.3
0.2
0.1
0
193
218
243
268
293
318
343
2
27
52
77
102
127
152
177
202
227
Day of year 2015-2016
SW
NE
Meadow

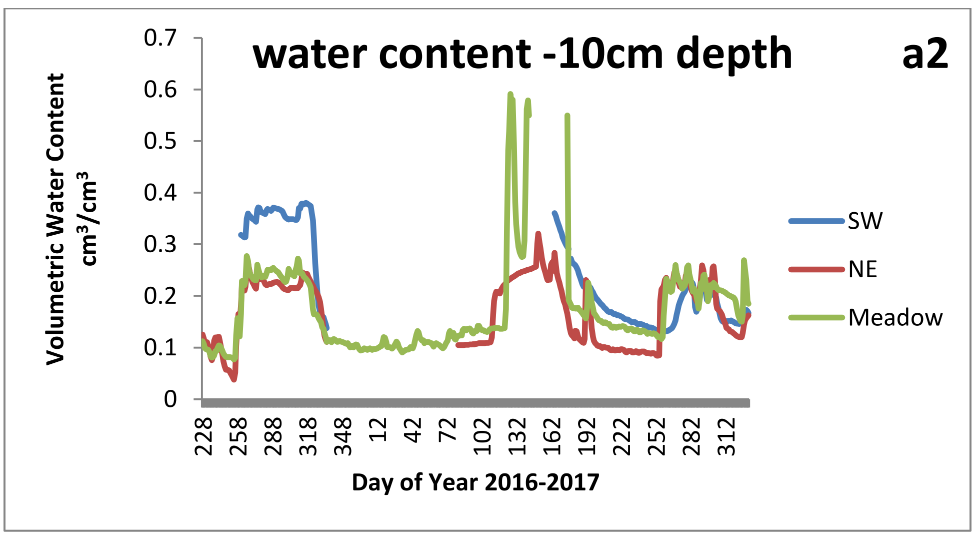
water content -10cm depth
a2
Volumetric Water Content cm³/cm³
0.7
0.6
0.5
0.4
0.3
0.2
0.1
0
228
258
288
318
348
12
42
72
102
132
162
192
222
252
282
312
Day of Year 2016-2017
SW
NE
Meadow

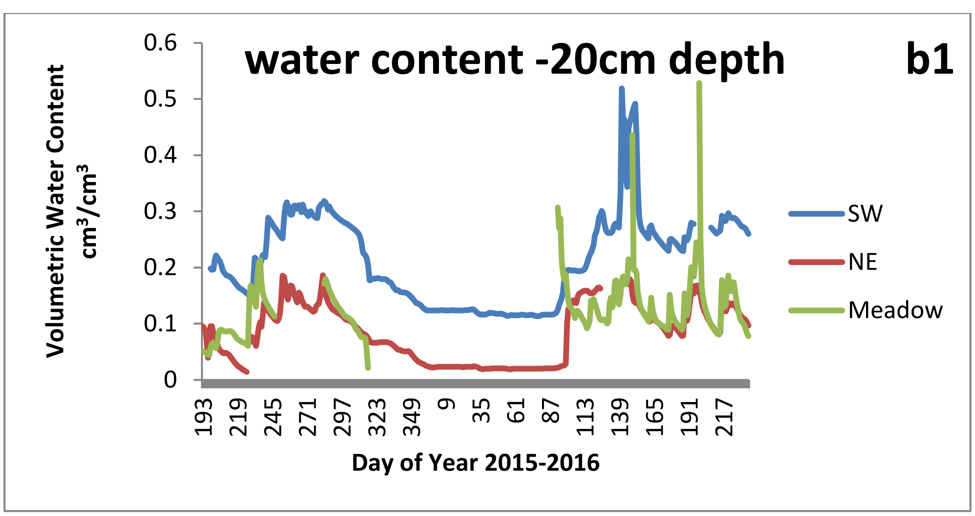
water content -20cm depth
b1
Volumetric Water Content cm³/cm³
0.6
0.5
0.4
0.3
0.2
0.1
0
193
219
245
271
297
323
349
9
35
61
87
113
139
165
191
217
Day of Year 2015-2016
SW
NE
Meadow

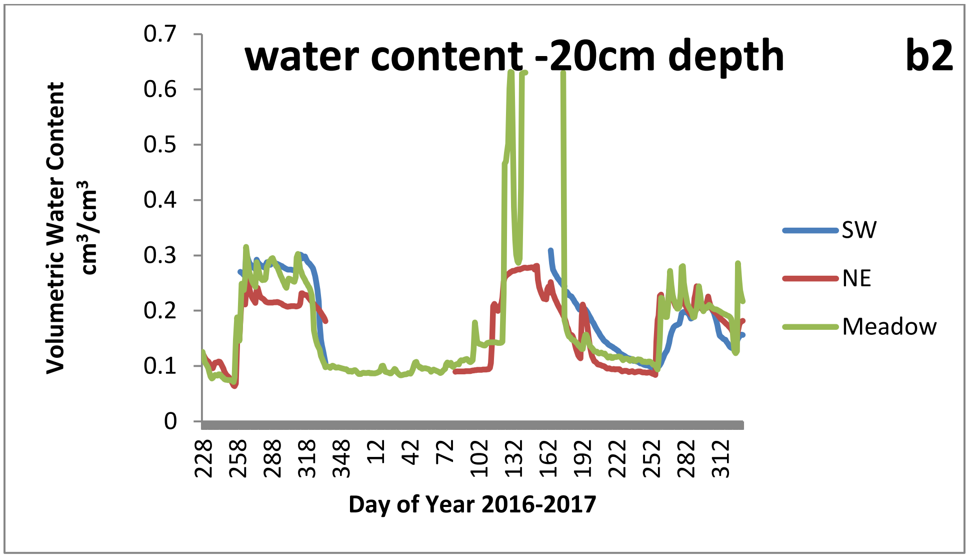
water content -20cm depth
b2
Volumetric Water Content cm³/cm³
0.7
0.6
0.5
0.4
0.3
0.2
0.1
0
228
258
288
318
348
12
42
72
102
132
162
192
222
252
282
312
Day of Year 2016-2017
SW
NE
Meadow

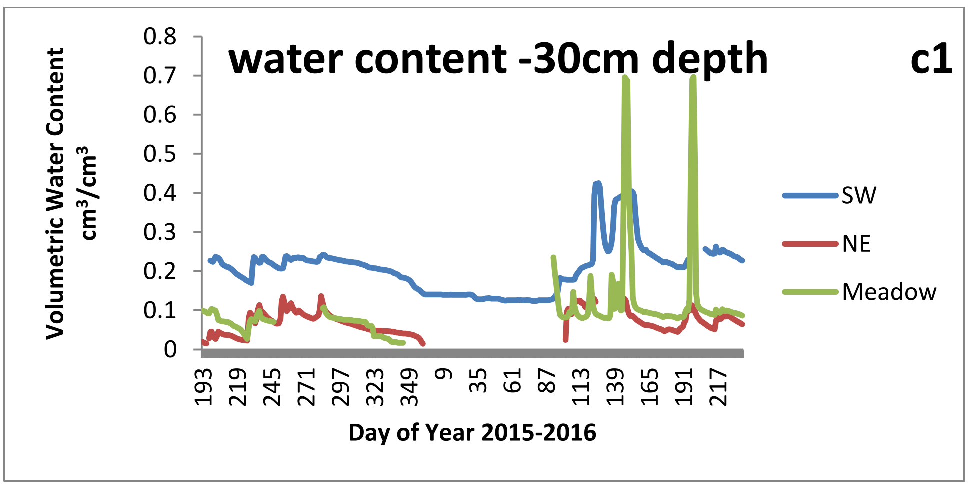
water content -30cm depth
c1
Volumetric Water Content cm³/cm³
0.8
0.7
0.6
0.5
0.4
0.3
0.2
0.1
0
193
219
245
271
297
323
349
9
35
61
87
113
139
165
191
217
Day of Year 2015-2016
SW
NE
Meadow

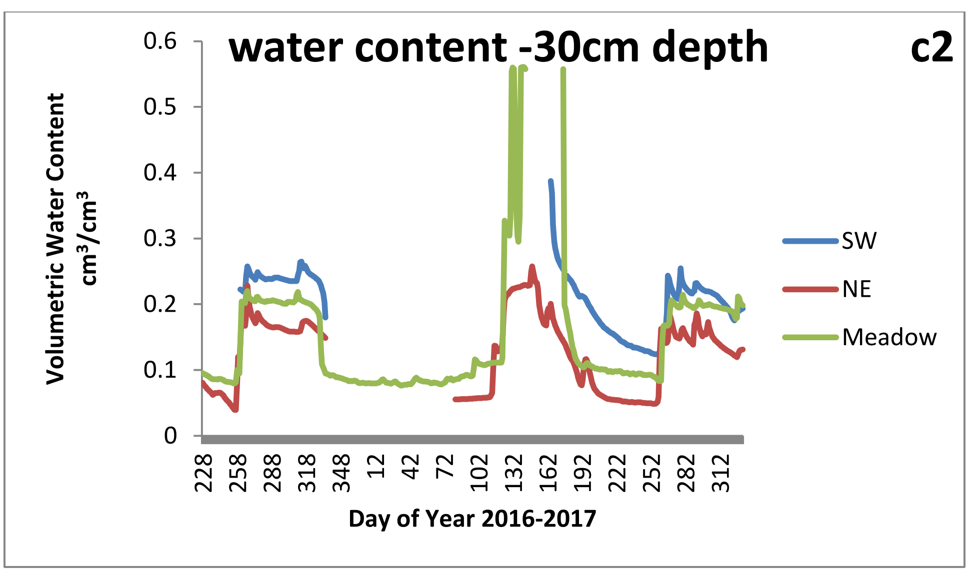
water content -30cm depth
c2
Volumetric Water Content cm³/cm³
0.6
0.5
0.4
0.3
0.2
0.1
0
228
258
288
318
348
12
42
72
102
132
162
192
222
252
282
312
Day of Year 2016-2017
SW
NE
Meadow

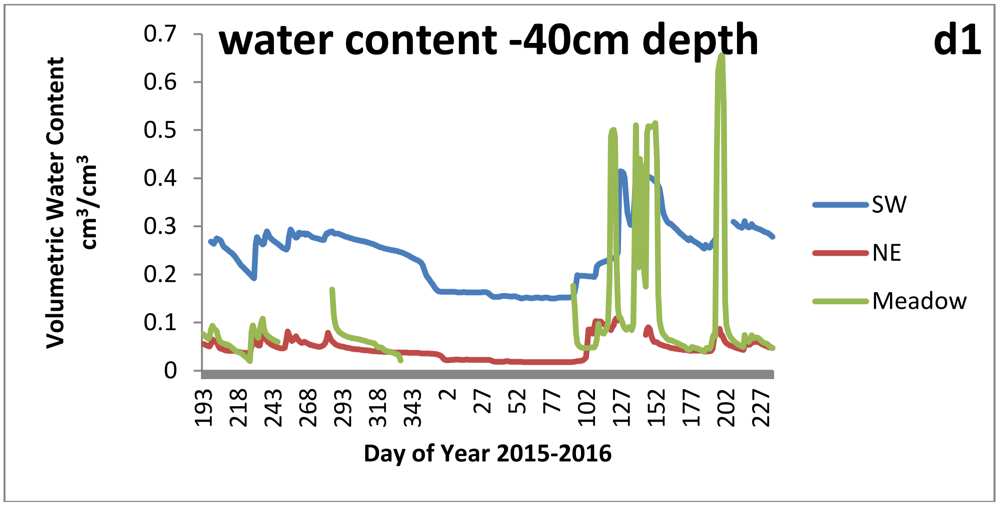

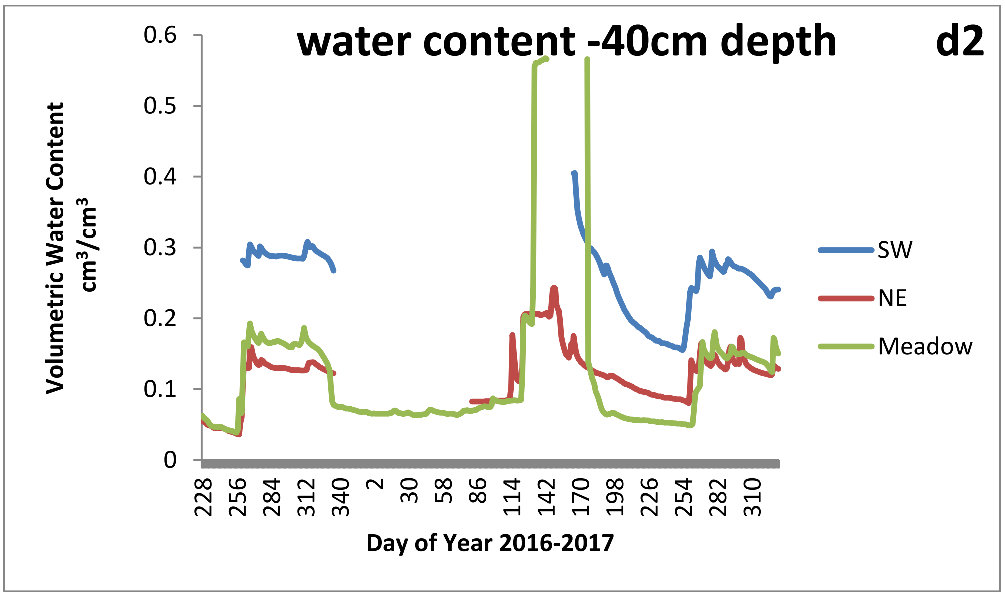

Figure 7 (a-d). Daily average volumetric water content at the forested study sites (SW and NE) and the unforested ridgeline (Meadow) at different depths from 11 July 2015 to 14 August 2016 (a1-d1) & from 15 August 2016 to 28 November 2017 (a2-d2). The missing pieces are due to instrument malfunction at the corresponding dates or freezing of soil in winter in case of the Meadow site.

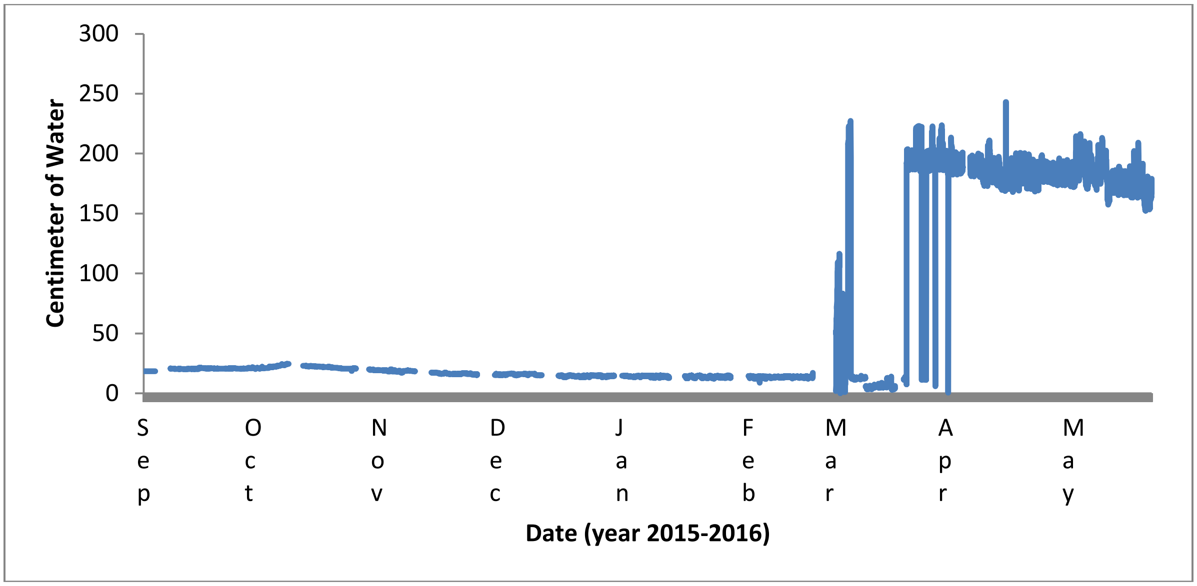

Figure 8. The flow of water in a first order stream that drains the study area flowing down the SW side from September 3, 2015 to May 19, 2016, measured using a pressure transducer.

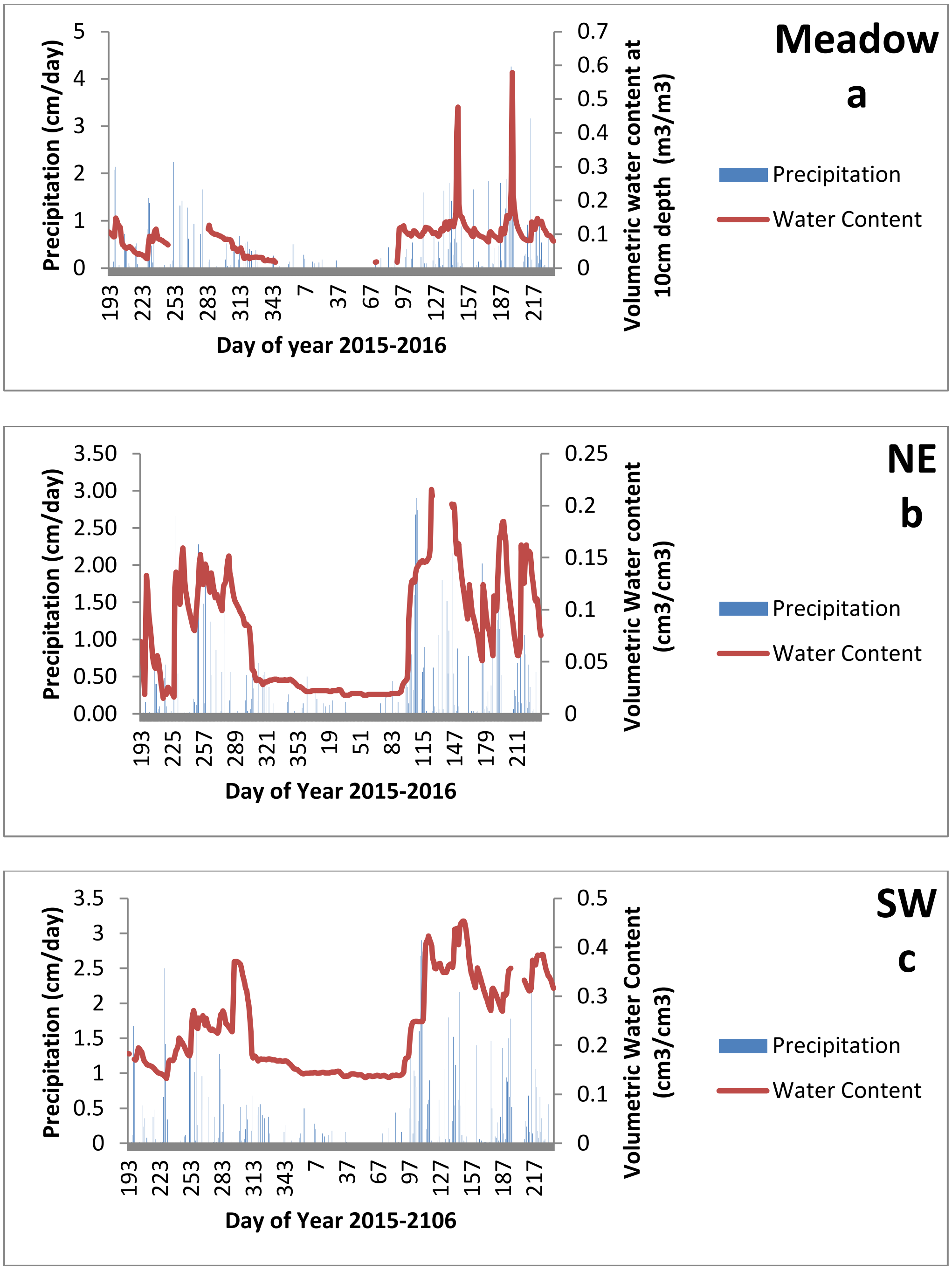

Figure 9 (a-c). Daily sum of precipitation and daily average volumetric water content at 10 cm depth from 11 July 2015 to 14 August 2016 for the Meadow, NE, and the SW sites. Winter months are noticeable by the flat line for water content.

Table 1. Initial and final soil moisture content, infiltration rates and saturated hydraulic conductivity (Ks) for all 3 study sites.

Site	Terrain	soil moisture (cm^3/cm^3)	Final Soil Moisture (cm^3/cm^3)	Infiltration rate (cm/h)	Ks (cm/hour)	Ks (cm/day)
Meadow	Vegetation	0.203	0.419	130.29	75.9	1821.6
Meadow	Vegetation	0.117	0.441	107.58	62.7	1504.8
Meadow	Stone Strip	0.068	0.342	90.30	52.6	1262.4
Meadow	Stone Strip	0.040	0.310	96.46	56.2	1348.8
Meadow	Stone Strip	0.050	0.389	99.30	57.9	1388.4
Meadow	Grassy Vegetation	0.085	0.431	119.16	69.4	1666.1
SW	Moss	0.224	0.400	40.44	23.6	565.4
SW	Dirt	0.269	0.415	80.61	47.0	1127.0
NE	Dirt	0.102	0.377	25.68	15.0	359.0
NE	Vegetation	0.103	0.387	25.15	14.7	351.6

Table 2. Ratio of the mass of gravel to mass of sediment <2mm, Clay, silt and sand, organic content (%), residual water content, saturated water content (cm^3/cm^3), Van Genuchten alpha, n and Saturated conductivity Ks (cm/day).

Site	G/S	Clay	Silt	Sand	Organic	θr	θs	α	n	Ks
Meadow	1.16	0.2	32.5	67.3	11	0.010	0.35	0.015	1.7	1400
NE	0.52	0.2	24.9	74.9	37	0.010	0.36	0.015	2.0	350
SW	0.45	17.1	41.4	41.5	30	0.015	0.46	0.015	1.7	565

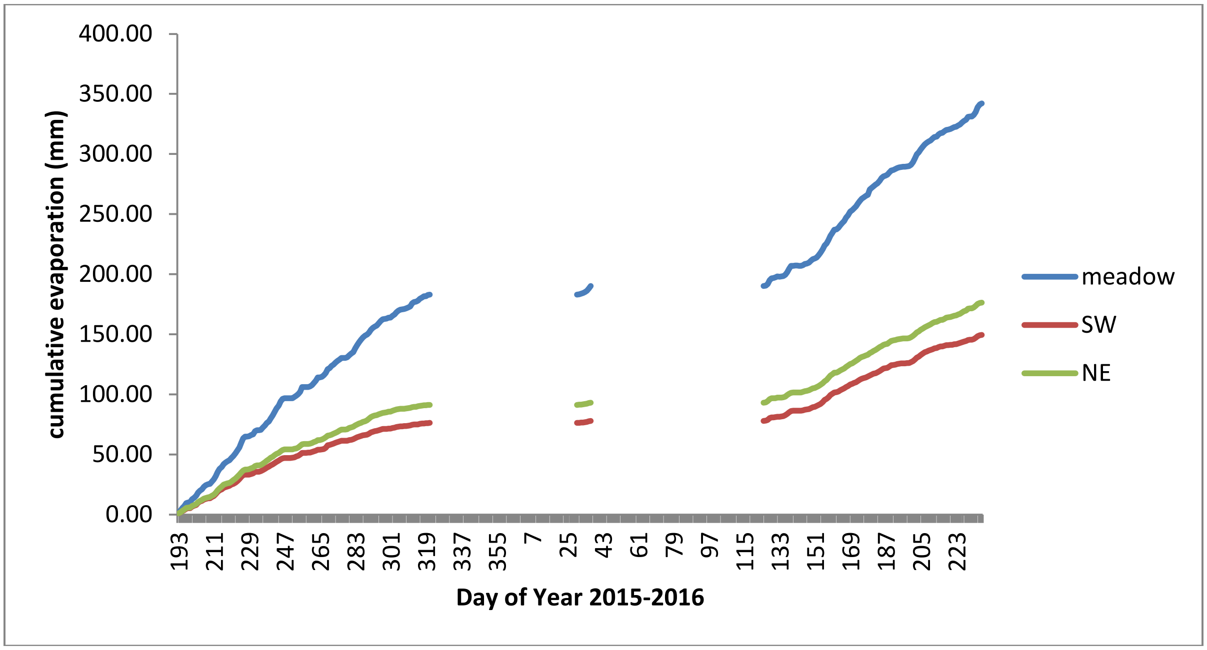

Figure 10. Modeled daily cumulative evaporation in mm using modified and adapted Penman Equation (2) for the Meadow, SW, and the NE sites from 11 July 2015 to 14 August 2016. Gaps in the figure are missing data from Nov 17, 2015 to Jan 30, 2016 and from Feb 7, 2016 to Apr 8, 2016 due to instrument malfunctions.

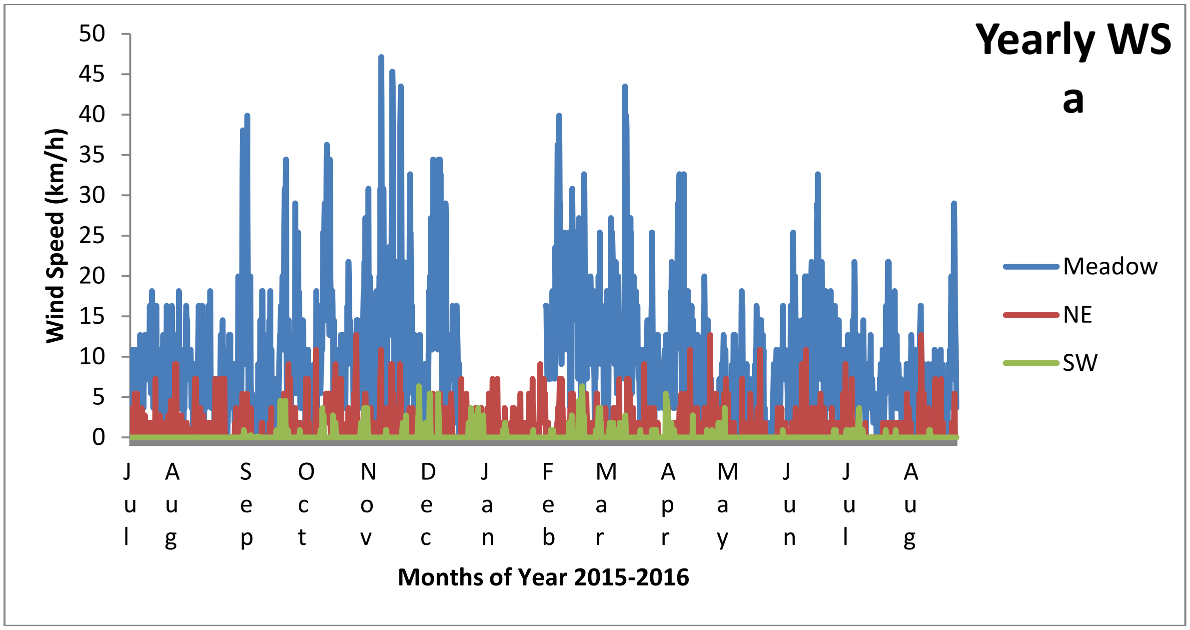

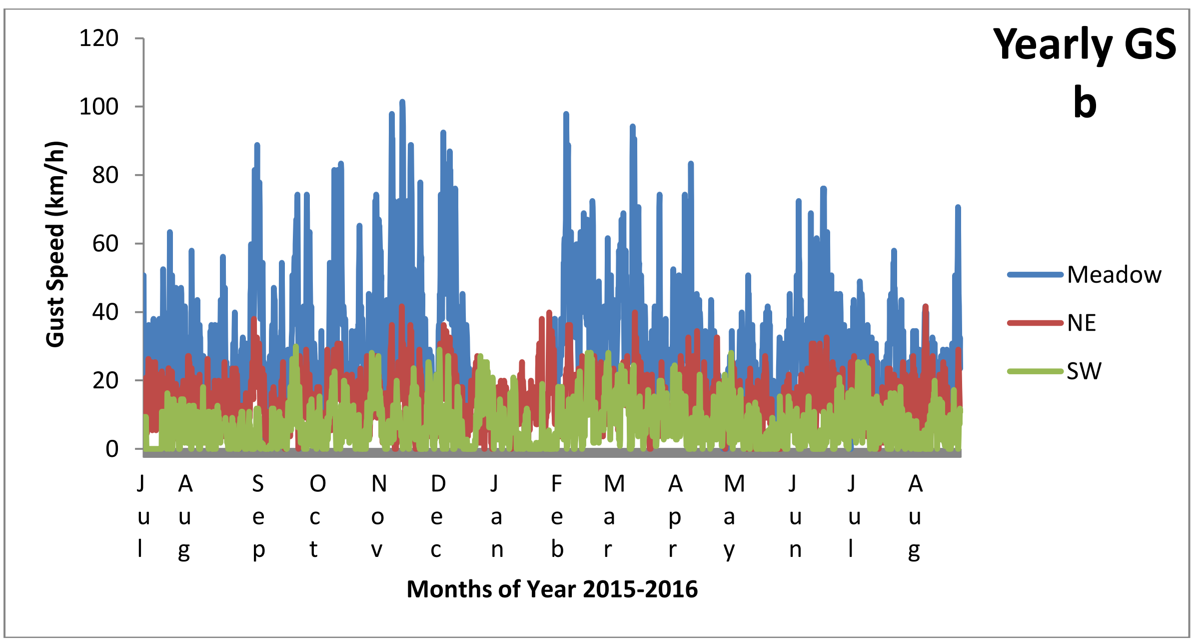

Figure 11. Measured wind speeds (a) and gust speeds (b) in km/hour for the Meadow, NE & SW for an entire year from July 2015 to August of 2016. The data from December 16 to January 30 are missing for the Meadow station, due to instrument malfunction.

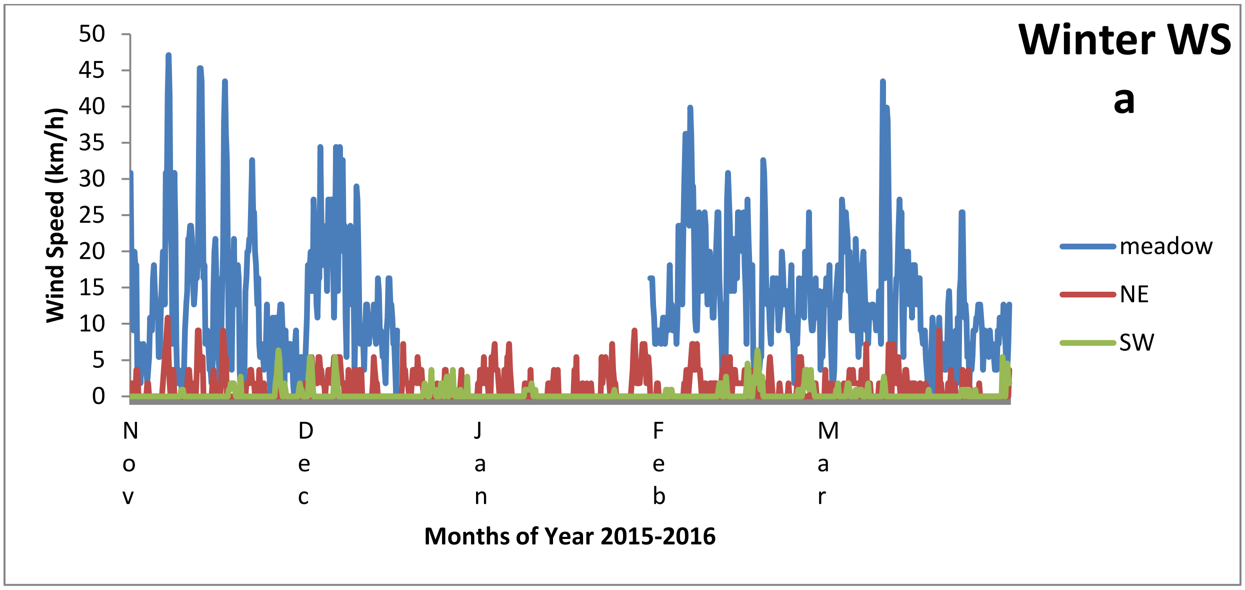

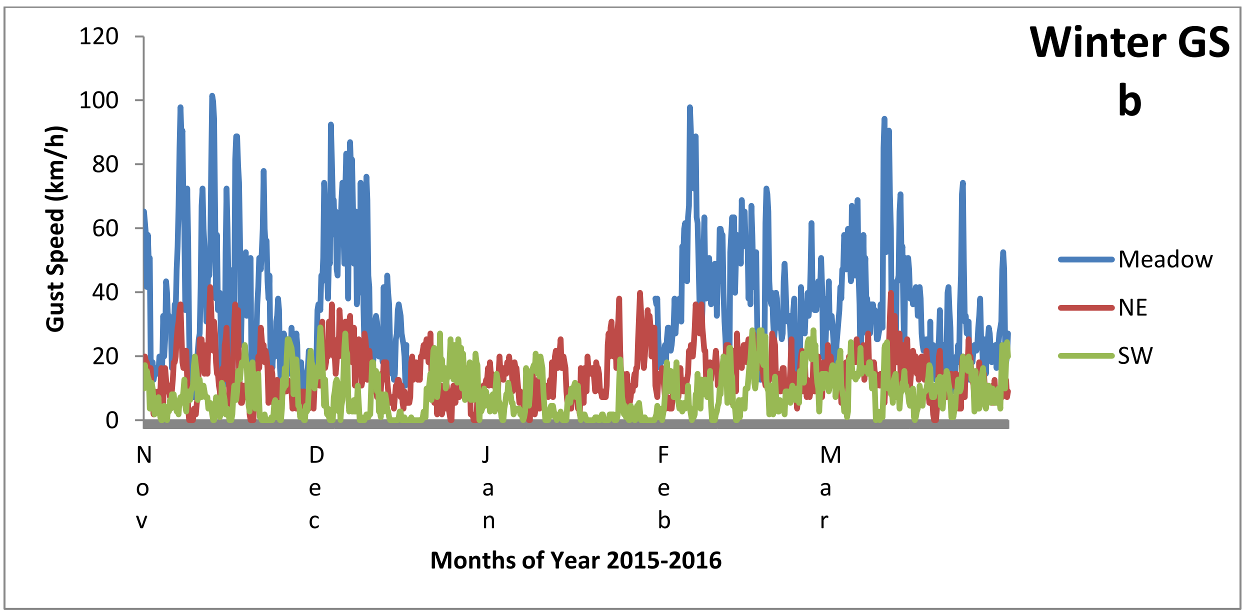

Figure 12. Measured wind speeds (a) and gust speeds (b) in km/hour for the Meadow, NE & SW for winter months only, from November 2015 to March of 2016. The data from December 16 to January 30 are missing for the Meadow station, due to instrument malfunction.

Matric Soil Water Potential

Modeled matric water potential of all three study sites (Figure 13) show that throughout the *growing season*, matric water potential remained low, which in turn means that water for plant uptake was available at all times. The SW site had the lowest water potential (best water availability), followed by the Meadow site. Interestingly, the NE site had the highest potential, particularly during the winter (February to March). The winter data are missing for the Meadow site (due to frozen soil) therefore, we cannot be certain that in fact NE has higher matric potential than Meadow during winter months. The matric potential for the Meadow and the NE sites follow each other closely the rest of the year. The Van Genuchten modeled matric regolith water potential in relation to the measured matric potential by tensiometers (Figure 14) has a Nash-Sutcliffe efficiency = 0.45. The efficiency coefficient is sensitive to extreme values and yields sub-optimal results when the dataset contains large outliers in it as ours does.

Seed Planting Experiment

To confirm that seedlings are not able to survive the winter after germination, in July of 2015 seeds of the three native species (*Pinus contorta, Picea Engelmannii* and *Abies lasiocarpa)* were germinated in the laboratory and along with ungerminated seeds were planted and sown at the ridge (Meadow) site in three different locations. Each location had nine plots, three plots for each species. In one plot, the seedlings were planted directly onto the vegetative surface. On the second plot the seedlings were individually planted into the soil and partially covered. On the last plot, the seeds were scattered along the surface. All plots were saturated with water after planting. After one year no survivors were found (May of 2016).

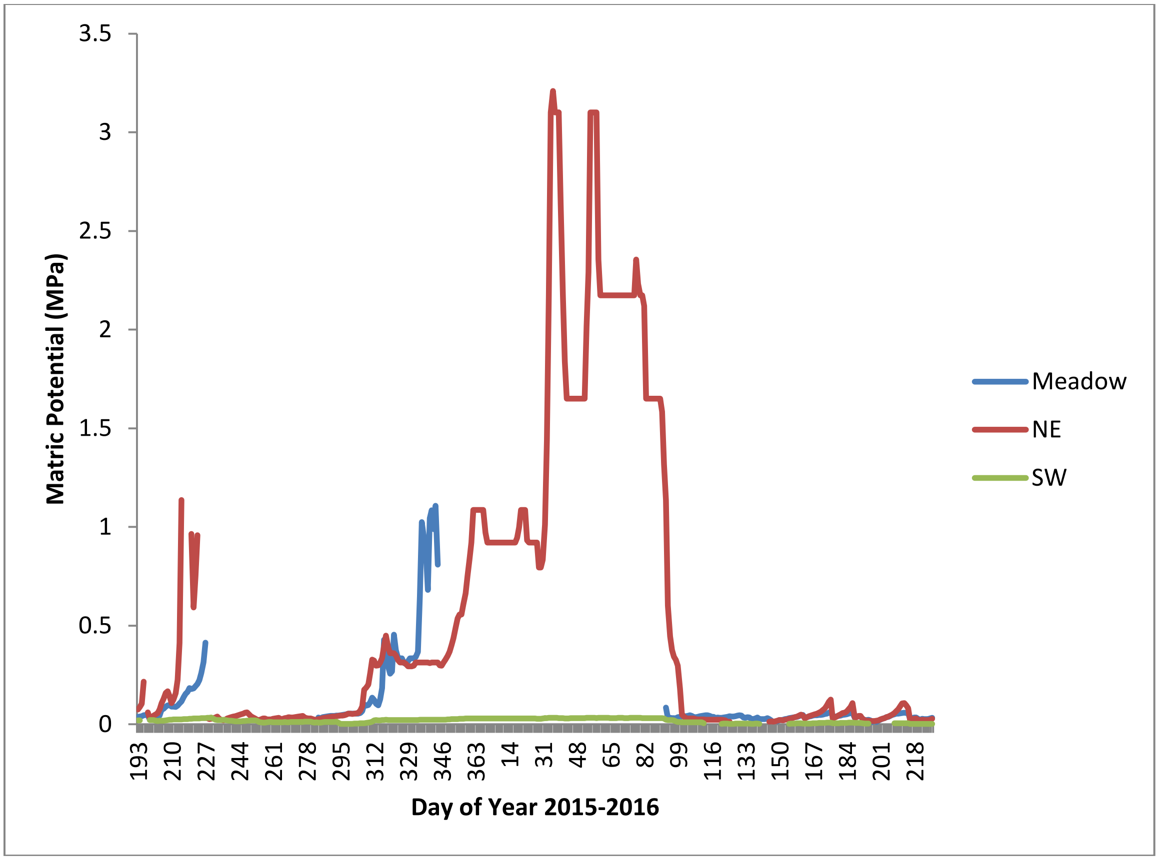

Figure 13. Modeled daily matric potential in MPa (values are negative) of the SW, NE and the Meadow sites from 11 July 2015 to 14 August 2016. The missing data for the Meadow site from December 2015 to March 2016 is due to frozen soil which in turn stopped theta probe instruments from logging.

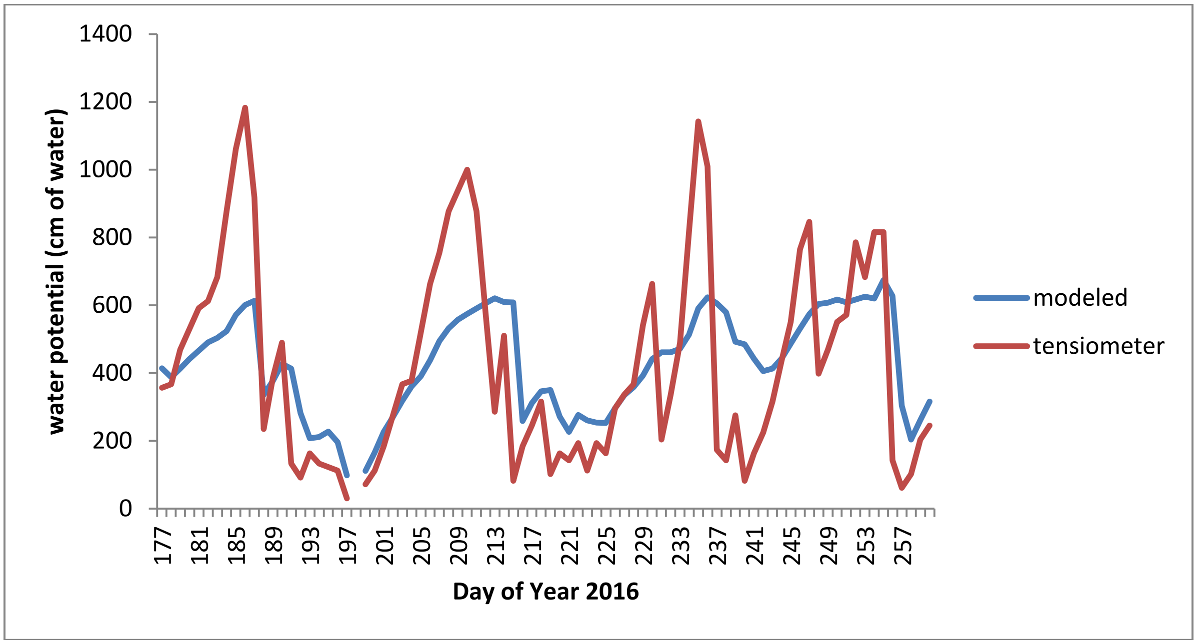

Figure 14. Meadow site comparison of the Van Genuchten modeled Equation (2) and the measured (tensiometers) matric regolith water potential in cm of water from Jun 25, 16 - Sep 16, 16. Nash-Sutcliffe efficiency = 0.45.

Table 3. Clay, silt, and sand content of the 15 stone stripes across the meadow of Jumping Pound Ridge.

SS #	1	2	3	4	5	6	7	8	9	10	11	12	13	14	15
Clay	0.2	0.1	1.3	0.4	0.1	1	0	NA	0.5	0.4	2.6	5	2.5	5.6	8
Silt	6.8	4.9	13.4	9.6	6.9	13.6	4	NA	8.3	7.1	20.4	20	21	42.8	60
Sand	93	95	85.3	90	93	85.4	96	NA	91.2	92.5	77	75	76.5	51.5	32

Table 4. Regolith characteristics and displacement of 15 painted squares on the Meadow of Jumping Pound Ridge.

Square ID	Location	Slope (°)	Average mass (g)	Distance-traveled[1] (cm)	Silt & clay content (proportion)	Thickness of fine debris layer[2] (cm)
1	Crest/NE	9	1.254	1.349	0.079	10
2	Crest/NE	9	0.391	2.147	0.056	15
3	Crest/NE	7	0.464	2.029	0.162	15
4	Crest/NE	7	0.311	1.196	0.113	13
5	Crest/NE	7	0.772	0.875	0.082	11
6	Crest/NE	7	0.240	2.009	0.159	15
7	Crest/NE	9	0.369	1.615	0.044	15
8	Crest/NE	6	0.110	0.932	0.100	13
9	Crest/NE	9	0.292	1.581	0.098	10
10	Crest/NE	9	0.258	1.554	0.081	15
11	SW slope	6	0.507	2.290	0.254	15
12	SW slope	6	0.501	2.045	0.301	13
13	SW slope	7	0.501	2.987	0.251	15
14	SW slope	4	0.761	2.108	0.532	11
15	SW slope	3	0.546	1.577	0.713	14

[1] Observation year 2015-2016
[2] Thickness of loose regolith within the uppermost 15 cm of sediments

The Empirical Frost-Heave Model

The empirical model (Equation 5 and 6) demonstrates that frost-heave does in fact occur on the Jumping Pound meadow (Figure 15). All the measurement parameters required for the model are presented in Table 3 & 4. The “effective” freeze-thaw or number of frost heave cycles per year (N) was calculated to be 58 cycles per year. The correlation between the calculated and observed movement is r= 0.86. There is an observed average regolith displacement of 1.75 cm/year and a modeled average regolith displacement of 1.67 cm/year.

Frost Heave Processes

Two necessary conditions are required for frost-heaving to take place. First condition (Equation 8), places a constraint on the characteristics that a soil must possess in order to be susceptible to significant heave. Based on these results, the first condition for frost heave holds in all three sites (Table 5).

The second condition requires an ice lens to be formed below the surface level and that can only come about if the temperature at the surface falls markedly below freezing of water while increasing with depth, reaching the melting temperature somewhere below the surface level where water in liquid form is gathered. The gathered water in the depth feeds the ice lens formed between it and the surface level, which in turn exerts an upward pressure. When this pressure due to the ice lens exceeds the pressure due to the weight of the ground above it, the surface is pushed upwards and falls over, resulting in frost heave.

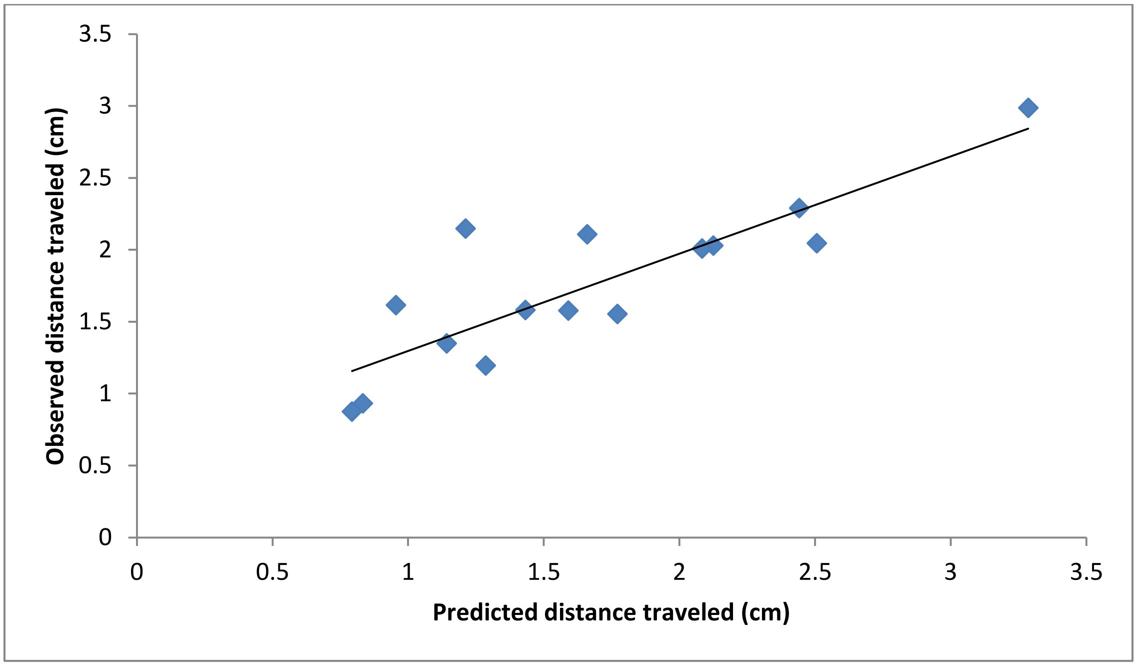

Figure 15. Distance traveled versus predicted distance of regolith. Surface velocity Vs as a function of the annual frequency of frost heave cycles N, the thickness of the top 15 cm of sediment D, the slope gradient θ and the silt and clay content of the layer SC. The correlation coefficient r is 0.86.

Table 5. The left hand side of Equation 8, Pore throat radius (m) vs. the right hand side (4φγsl/Po) J/m^2/kPa. The conditions of the equation is satisfied for all sites as Rp ≤ 4φγsl/Po.

Soil Characteristic	Meadow	NE	SW
Rp (pore throat radius)	2^{-6}	3^{-6}	6^{-7}
4φγsl/Po (J/m^2/kPa)	6.475^{-4}	6.36^{-4}	8.24^{-4}

In general, the temperature in approximately the first meter of soil is sensitive to the diurnal cycles of air temperature and solar radiation (Ashrae 1991) and can exhibit diverse patterns of change. Within this surface layer, temperature profiles can vary depending on the time of day or the temperature at the surface. When the soil surface temperature is very low, as in winter with no snow insulation, the temperatures increases linearly with depth. In summer, the profile is reversed due to warmer air temperatures and higher solar radiation (Andersland and Landanyi 2004). However, when the surface temperature is low but not too low, as in lower elevations, temperate regions or when there is a snow cover, the temperature profile in the first meter of soil exhibits a lot of variation and can change considerably based on the time of day. For example, in a study done in Nicosia, Cyprus, the temperature profile at 6 am is the opposite of the temperature profile at the same layer at 12 pm. At 6 am, the temperature was slightly warmer in the first 20 cm of the soil, got colder at about 50 cm and warmer again after that depth. The reverse was true at 12 pm (Florides & Kalogirou 2005). The temperature profiles depicted in figures 16 and 18 of our SWand NE sites respectively are reverse of one another similar to the temperature profiles for the 2 different times of days in the above mentioned study. As in the latter, the daily average temperature used for these two sites are different corresponding to the slight difference between the temperatures at 6 am and noon.

The other relevant factor determining the overall shape of the temperature profile in these two sites could be the pattern in distribution of the soil moisture. The changes in the temperature profiles of both sites follow the pattern of changes in their corresponding water content profile but in reverse order. That is to say, as the soil moisture increases the temperature decreases. The inverse relationship between moisture and temperature has been previously shown in multiple field and laboratory studies (e.g Lakshmi et al. 2003 & Chanzy et al. 2012). Furthermore, the changes in temperature is very sensitive to the changes of the soil moisture content, in that slight changes in water content results in much larger changes in the temperature differences. In deeper layers, the cyclic variation becomes dampened, more so in the water content as in the temperature values (Chanzy et al. 2012).

Our data points for temperature and water content match this relationship, and the interpolated graphs show a similar pattern of change between temperature and water content profiles (Figures 16-20). The shape of profiles for the SW site depicted in Figures 16 show an initial smooth increase in temperature followed by a smooth decrease and reversal at around -20 cm. The water content profile in Figure 17 exhibits the same pattern in reverse, albeit within a much more limited range of values, the change of direction occuring at around the same depth point of -20 cm.

The temperature and water content profiles in the NE site show both a more complicated behaviour. As is evident in Figure 18, the temperature decreases initially, turning around at -20 cm and increasing until around the depth of -30 cm, then decreasing again afterward. The water content profile (Figure 19) for the two data points in the months of November and December exhibit a more or less similar pattern only in reverse, increasing first and then decreasing rapidly at around -20 cm and then slowing down considerably and creating a point of inflection at around -30 cm.

Unfortunately, the measurement of the water content for depths between -20 cm and -40 cm are missing for the next corresponding data points in the months of January to March. However, the profile for days prior to January (Figure 20), where the data points for these depths are available, continue to show the same overall shape for the water content profile. Finally, it is worth mentioning that these temperature fluctuations are still relatively small as compared to the range of temperature variation in the meadow region. Because of all these factors, the profiles do not satisfy the necessary conditions for frost heave as predicted in our theoretical model.

Unlike the NE and the SW sites, the ground surface of the meadow site is not covered with snow most of the year for more than a short time. During the colder parts of the year, the temperature at the ground level is markedly below the freezing point of water and matches the description in Andersland and Landanyi (2004), with the temperatures increasing with depth linearly in various steps.

The results of the daily average temperature measurements at the depths of -10 cm, -20 cm, -30 cm and -40 cm were collected as two sets of data points corresponding to two consecutive years. The data from June of 2015 to the June of 2016 comprised one data set, and the data from June of 2016 to the end of May 2017 in the second data set. The relevant data points for analysing the occurrence of frost heave are the data for the cold months of the year, approximately from the middle of November to the end of March, and these are the periods to which we primarily turn our attention in this section.

As described in the method section, the temperature profile were extended by interpolating the temperature values between the four discrete data points using MATLAB's interp1 function and the PCHIP method, and extrapolating the temperature function from the surface to where temperature reaches $T=T_m$, the freezing/melting temperature of water.

The ensuing temperature graphs match the theoretical temperature profile in the presence of frost heave during the cold period of both years. In particular, the resulting graphs depict a continuous function comprised of three distinct regions of near linear dependence of depth with temperature. An example of the temperature profile and the estimate for January 2016 is depicted in Figure 21.

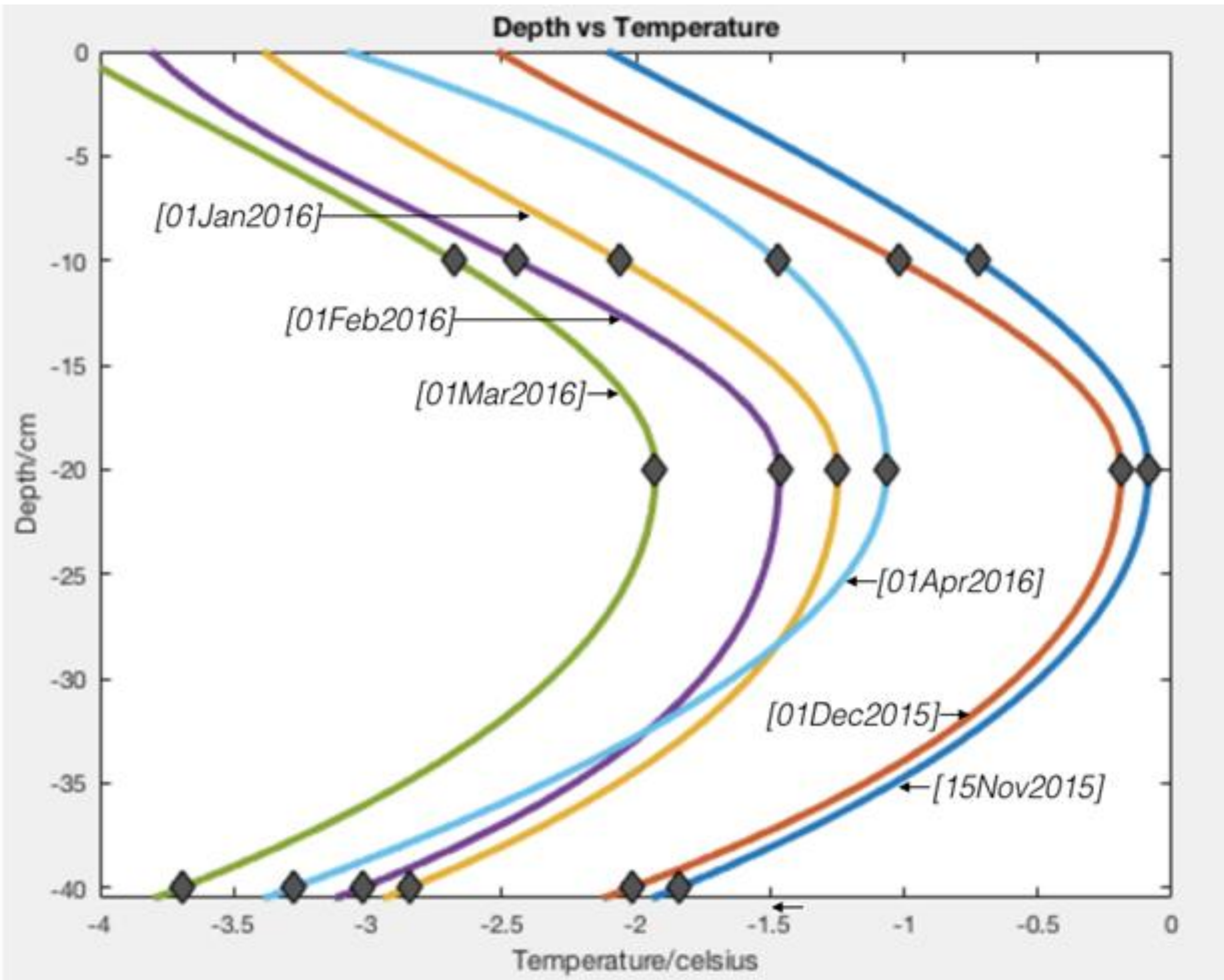

Figure 16. Temperature Profile at the SW site for the 15 November 2015 (blue), 1 December 2016 (red), 1 January 2016 (yellow), 1 February (purple), 1 March (green) and 1 April 2016 (cyan). The points on the graph are the measured values.

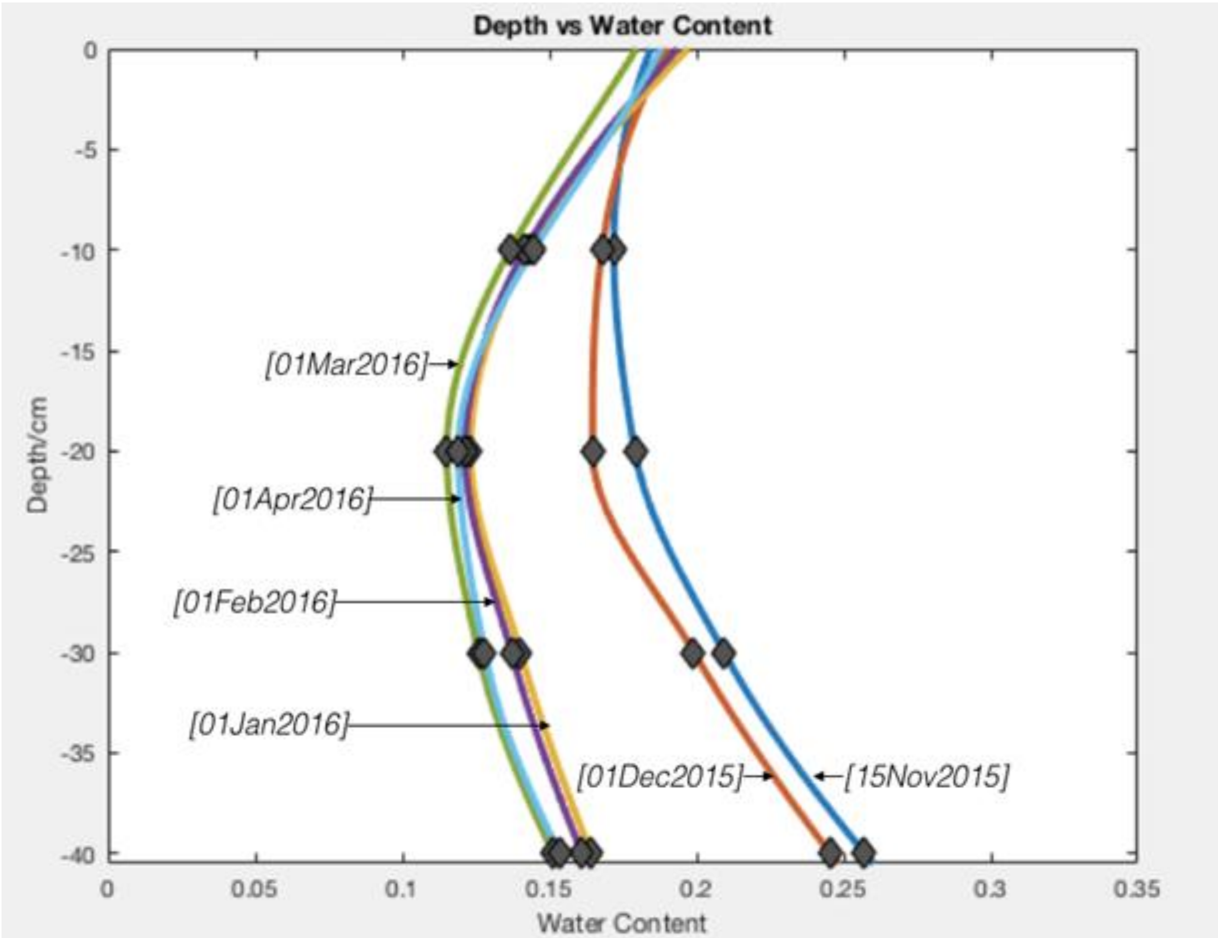

Figure 17. Soil water content with depth at the SW site for the 15 November 2015 (blue), 1 December 2016 (red), 1 January 2016 (yellow), 1 February (purple), 1 March (green) and 1 April 2016 (cyan). The points on the graph are the measured values.

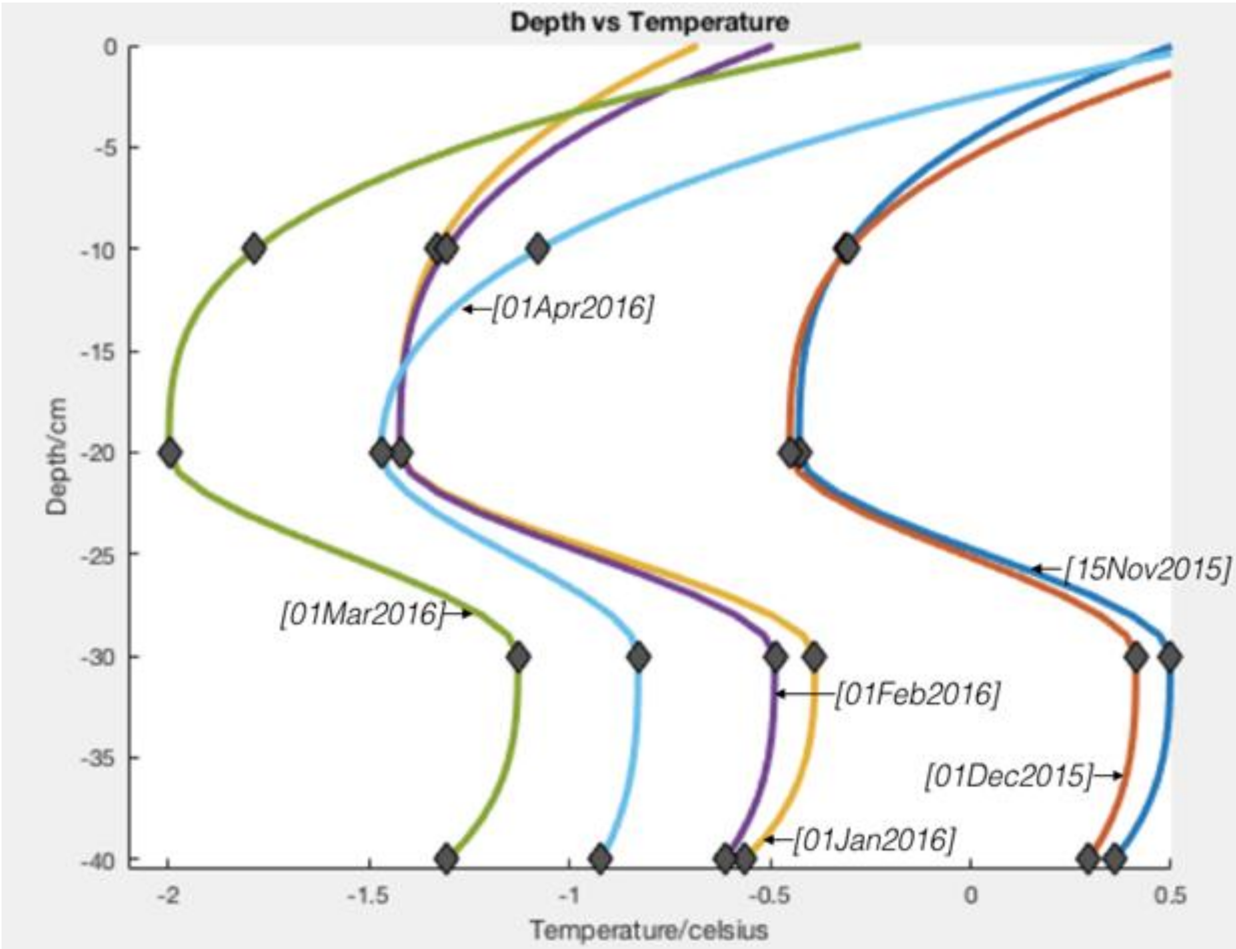

Figure 18. Temperature Profile at the NE site for the 15 November 2015 (blue), 1 December 2016 (red), 1 January 2016 (yellow), 1 February (purple), 1 March (green) and 1 April 2016 (cyan).The points on the graph are the measured values.

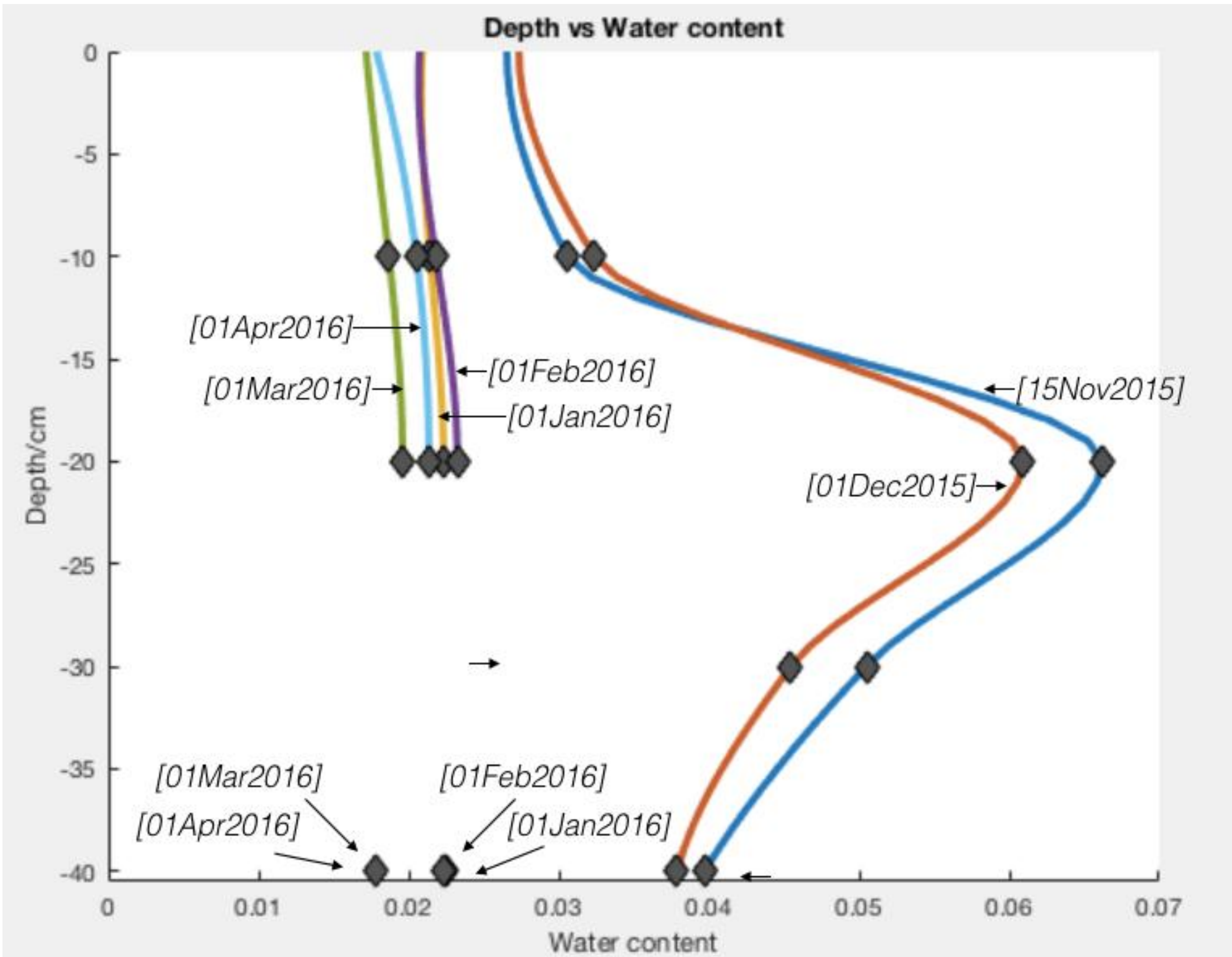

Figure 19. Soil water content with depth at the NE site for the 15 November 2015 (blue), 1 December 2016 (red), 1 January 2016 (yellow), 1 February (purple), 1 March (green) and 1 April 2016 (cyan). The points on the graph are the measured values.

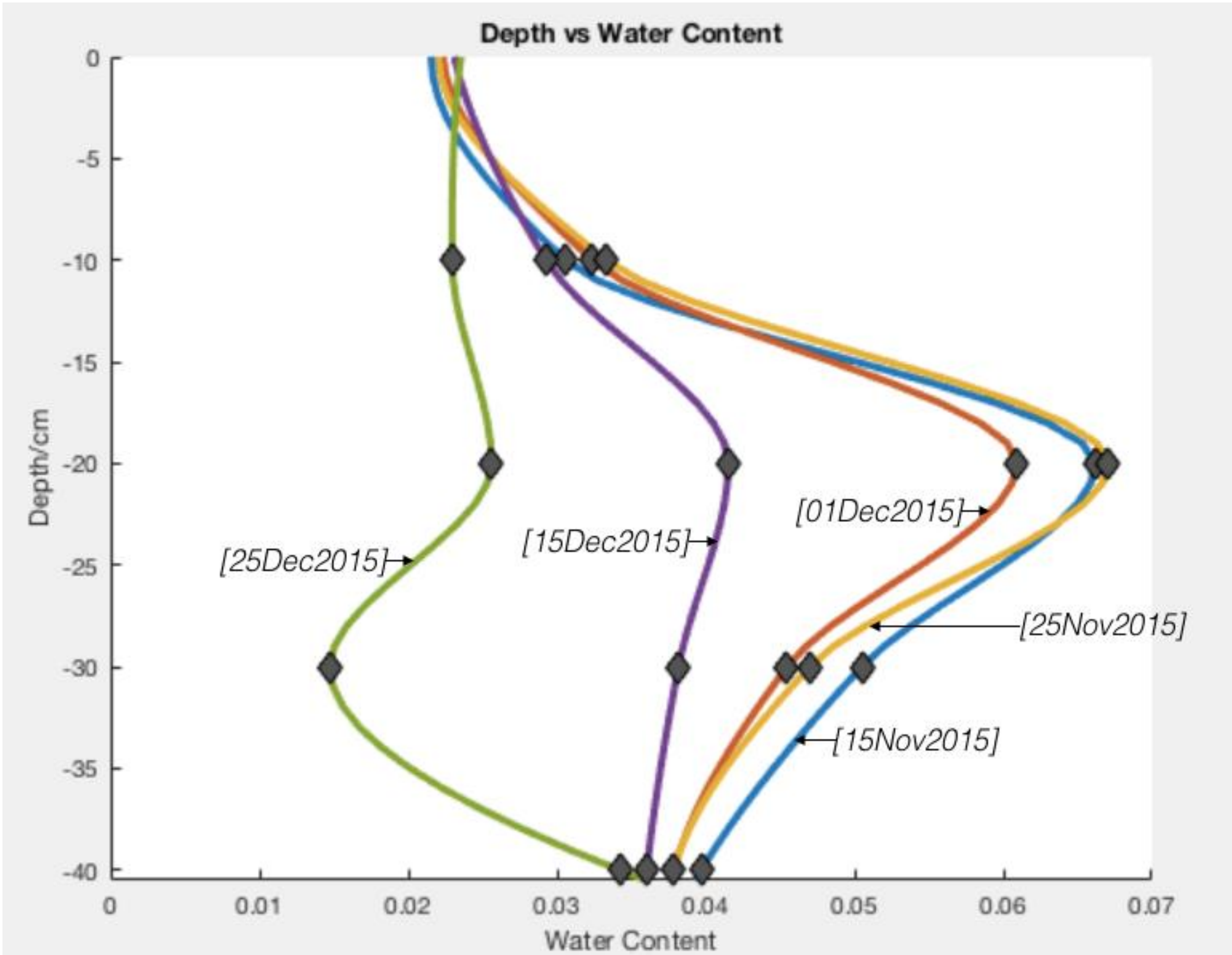

Figure 20. Soil water content with depth at the NE site for the 15 November 2015 (blue), 25 November 2015 (yellow), 1 December 2015 (red), 15 December 2015 (purple), 25 December 2015 (Green).

Analysis of the graphs for the days within the first data set (ie. the period of November 2015 to March 2016) demonstrate that the first region starting from the surface has the smallest slope. The second region corresponds to a steeper slope starting around z=-10cm. Finally the third region starts around z=-35 cm with still higher slope (compare Figure 21 and Figure 5). We estimated the values for the depth at which the ice lens forms, $z=z_L$, and the corresponding temperature $T=T_L$ as well as the depth at which the frozen fringe is formed $z= z_F$ and its corresponding temperature $T=T_F$, based on the abovementioned points of slope change. We conclude that although the value of z_L varies slightly on a daily basis, it remains close to the average value of z_L=-10 cm. Similarly, the value of z_F stays around the average value of z_F=-35 cm. Additional examples of the temperature profile graphs for various days during fall and winter where frost heave is expected to take place are shown in Figures 22-25, all of which share the same main features discussed here.

The results from the second data set (ie. the period between November 2016 to March 2017) are consistent and exhibit the same overall pattern. A sample graph for the first day of the months within this period is depicted in Figure 27. A similar analysis of the average daily temperatures within this data range points to a value of z_L around z_L=-10 cm, and slightly thicker frozen fringe extending from z_L=-10 to z_F=-40 cm.

By determining the values of z_L and z_F, we can identify the three layers predicted by our theoretical model, namely the ice lens, the frozen fringe and the unfrozen soil below it.

In the final step, as was discussed in the methods section, we calculate the upward pressure P_{max} and compared it with the downward pressure P_0 coming from the weight of the top layers of the ice lens. Our calculated pressure profile does demonstrate that this is the case for most of the days within the above period of study. The graph of the pressure P_{max} versus days of the month for the first data set (2015-2016) is depicted in Figure 26. Superimposed on the graph is the benchmark value of P_0 for the meadow region. Similarly, the graph of the pressure P_{max} versus days of the month for the second data set (2016-2017) is depicted in Figure 28. As before, the overall pattern is the same during both periods, with approximately the same range of days matching the frost heave model. The graph of the second data set (Figure 28) contains data for later months of April and May 2017. It is evident that the P_{max} pressure falls below the downward pressure P_0 during these months. In other words, as the daily temperatures rises with the advent of spring, the data predicts no frost heave based on our model, as is consistent with our expectation. The conclusion is that the detailed temperature and intermolecular pressure profiles calculated from the measurement data supports the existence of frost heave during the period of November to March on the meadow. The results are consistent with the results of the measurements of displaced and flipped stone stripes within designated squares reported in the frost heave measurements of the empirical model section, and together they provide strong evidence for the existence of frost heave on the meadow region on a yearly basis during the fall and winter months.

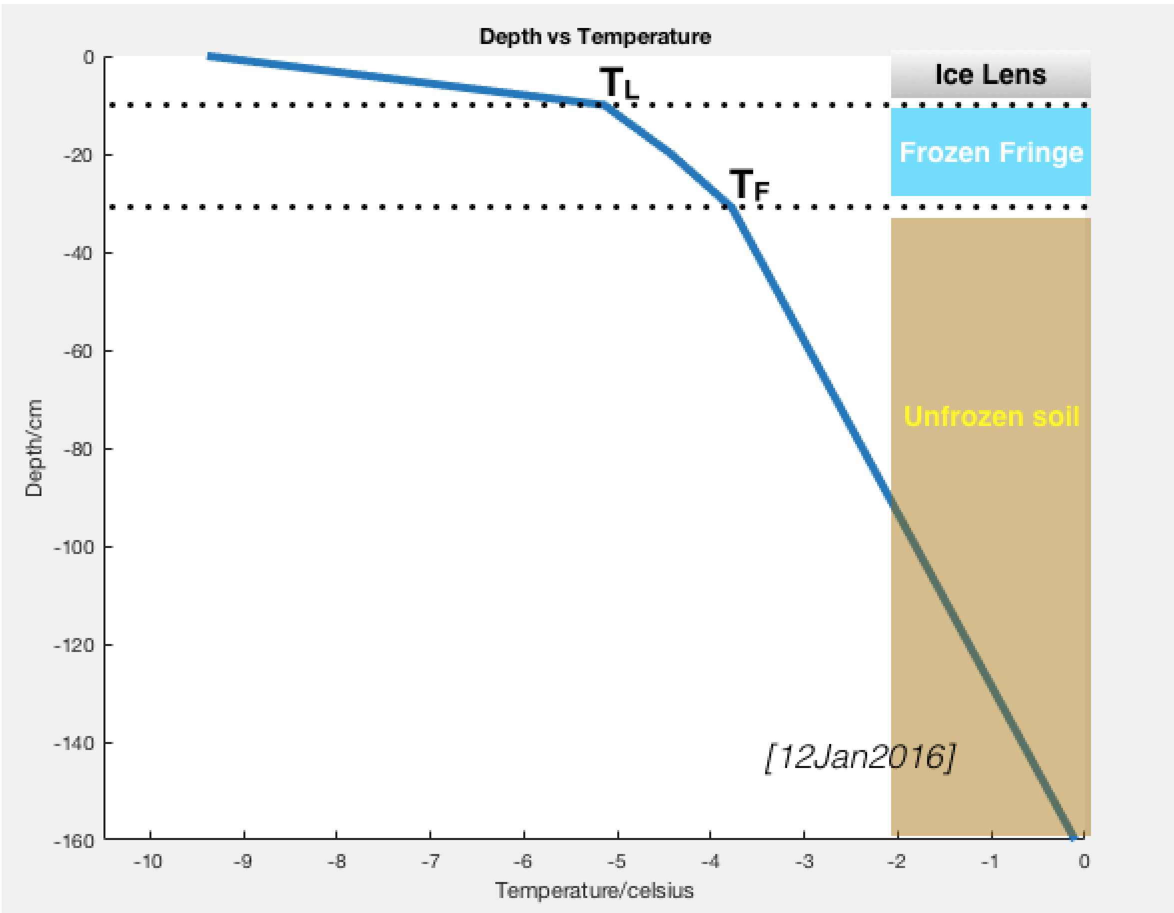

Figure 21. Temperature profile for 12 January 2016 of the Meadow site. The temperature is below the melting temperature for ice and gets warmer at deeper points. The graph matches the conditions for frost heave. The temperature point denoted by T_L is the temperature at the ice lens formation layer. The temperature T_F denotes the temperature at the start of the frozen fringe.

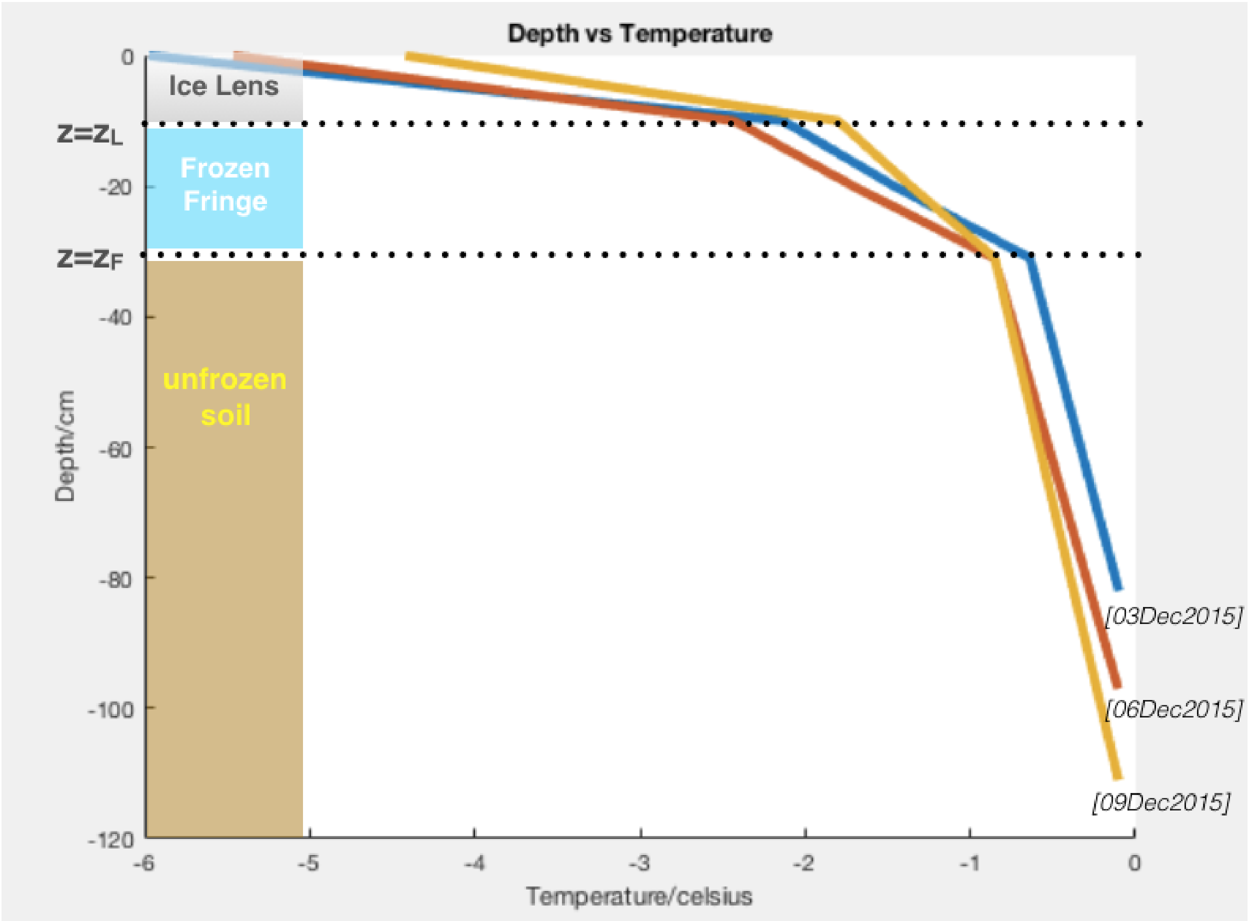

Figure 22. Temperature Profile at the Meadow site for 3 nearby days, ie. the 3, 6 and 9 of December 2015. The temperature is below the melting temperature for ice and gets warmer at deeper points. The estimate for the depth at which ice lens forms is denoted by $z=z_L$. The frozen fringe forms at $z=z_F$. The graphs match the conditions for frost heave.

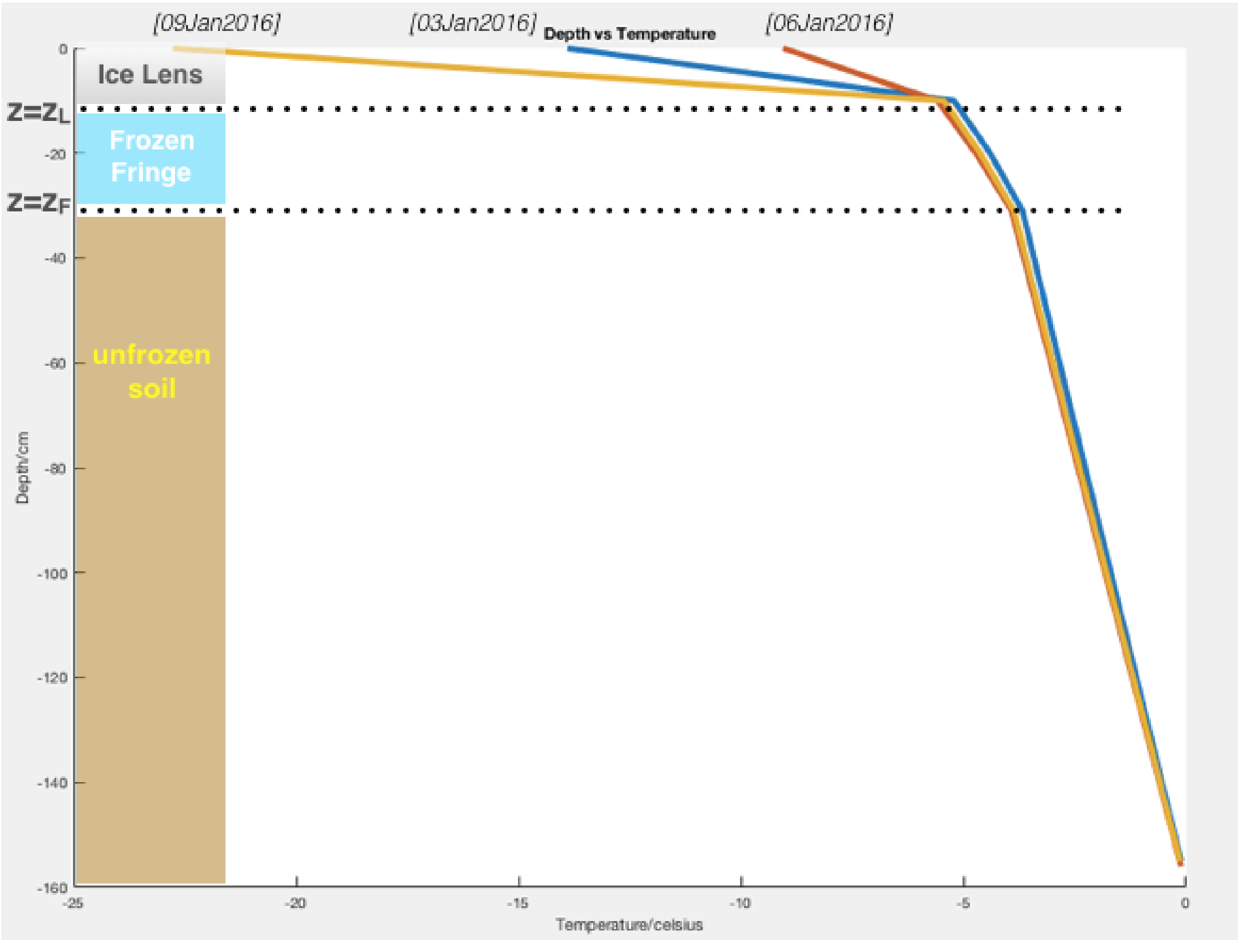

Figure 23. Temperature Profile at the Meadow site for 3 nearby days, ie. the 3, 6 and 9 of January 2016. The temperature is below the melting temperature for ice and gets warmer at deeper points. The estimate for the depth at which ice lens forms is denoted by $z=z_L$. The frozen fringe forms at $z=z_F$. The graphs match the conditions for frost heave.

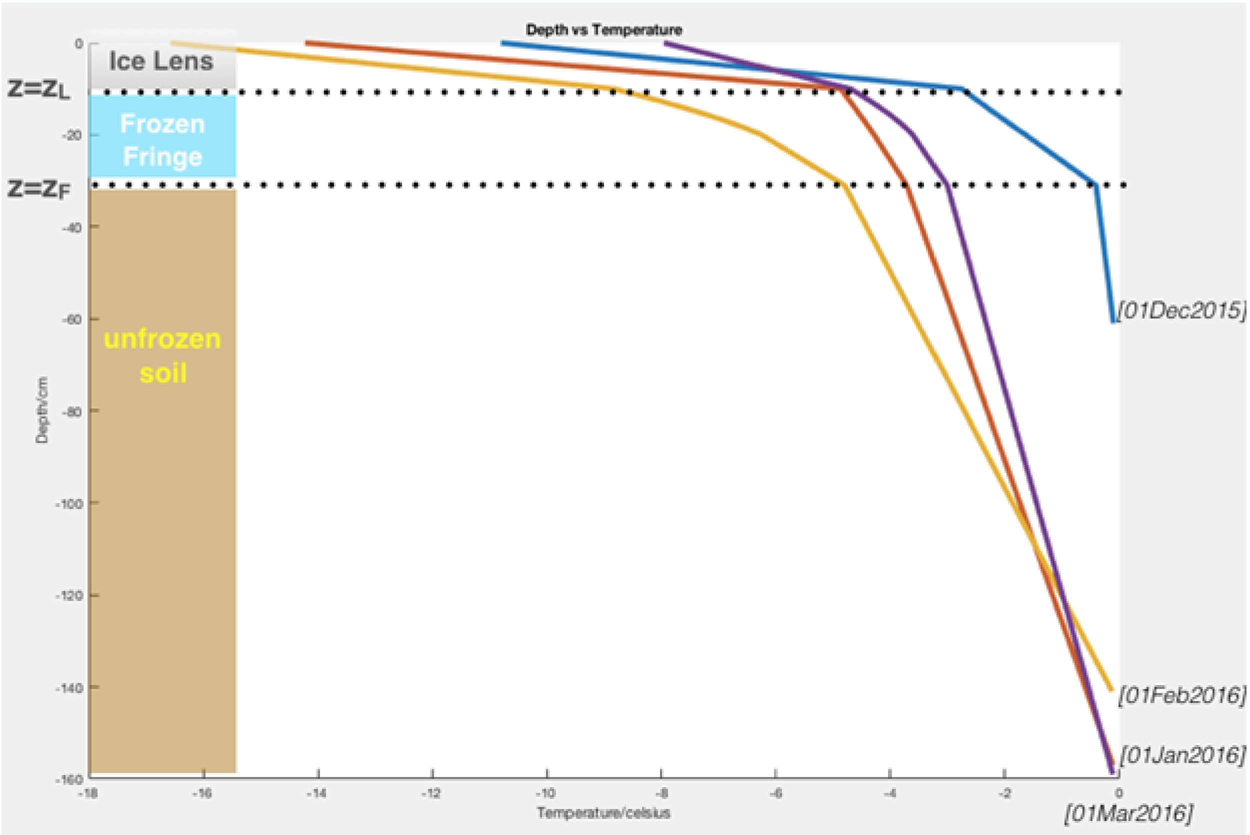

Figure 24. Temperature Profile at the Meadow site for the first of the months December 2015 to March 2016. The temperature is below the melting temperature for ice and gets warmer at deeper points. The estimate for the depth at which ice lens forms is denoted by $z=z_L$. The frozen fringe forms at $z=z_F$. The graphs match the conditions for frost heave.

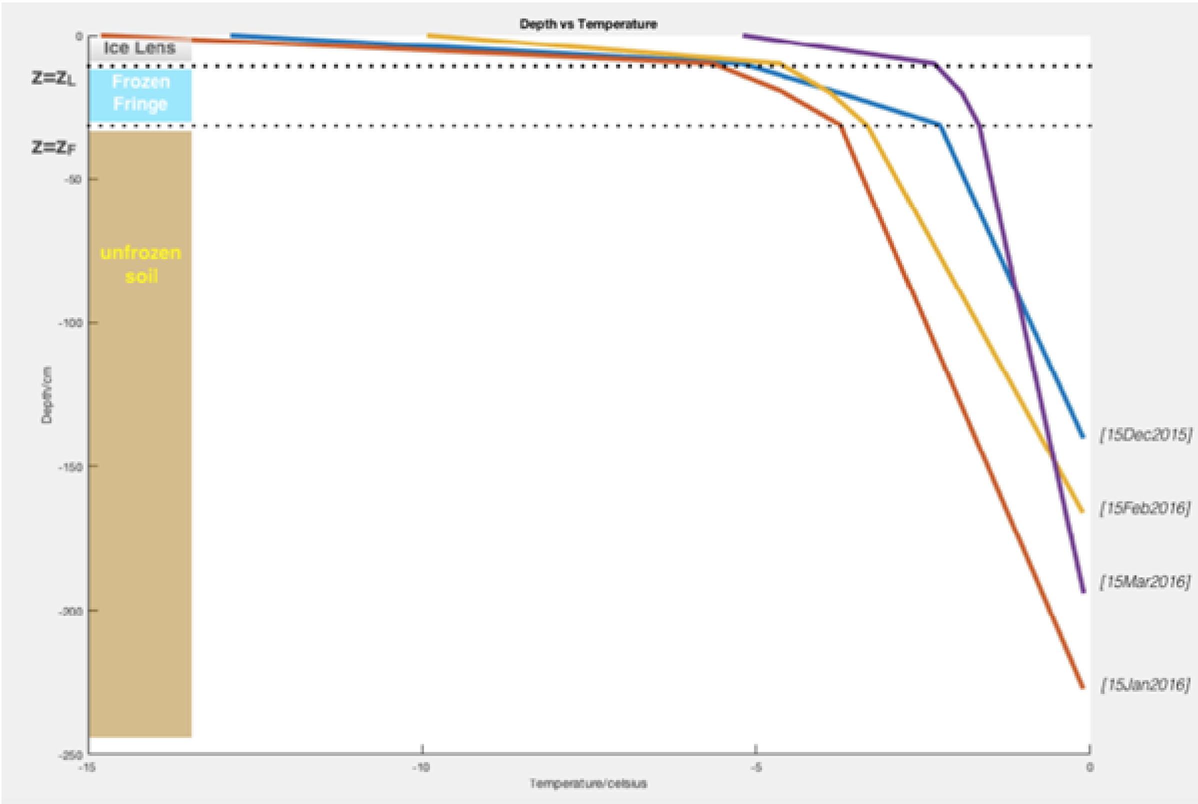

Figure 25. Temperature Profile at the Meadow site for the 15 of the months December 2015 to March 2016. The temperature is below the melting temperature for ice and gets warmer at deeper points. The estimate for the depth at which ice lens forms is denoted by $z=z_L$. The frozen fringe forms at $z=z_F$. The graphs match the conditions for frost heave.

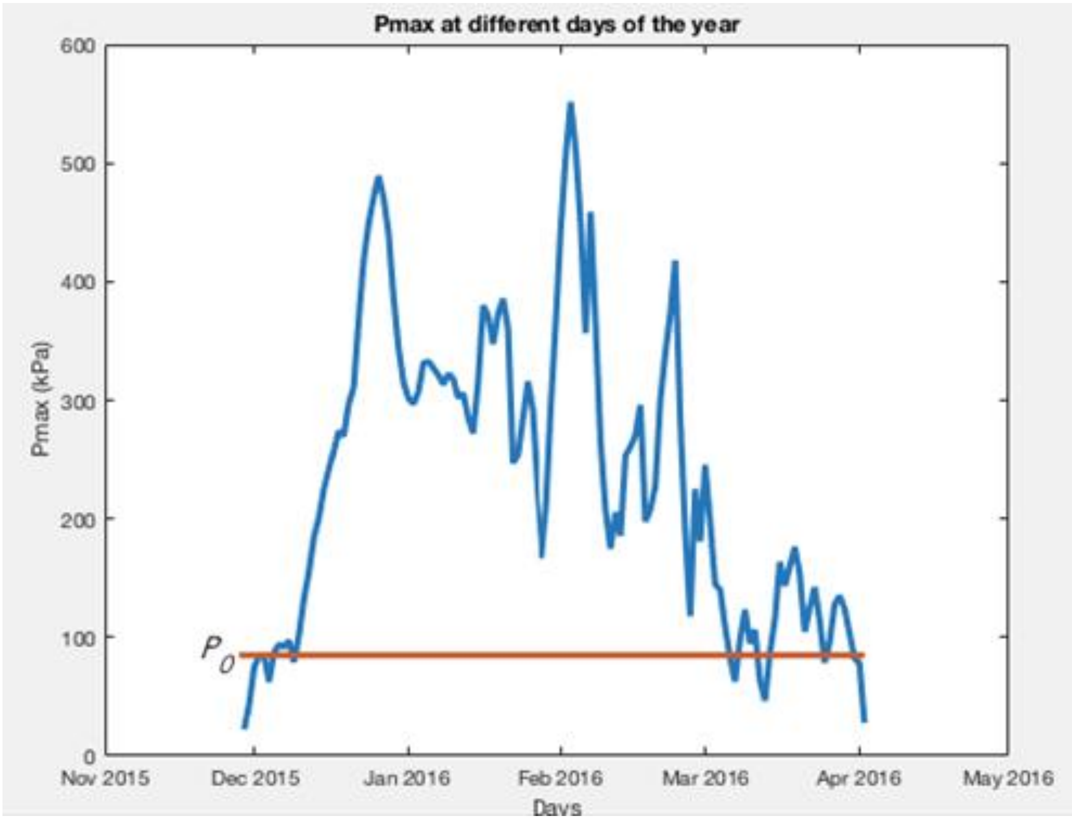

Figure 26. The graph of maximum intermolecular pressure measuredduring the period of 28 November 2015 to 2 of April 2016 at the Meadow site. The red line indicates the constant downward pressure on the surface based primarily on the elevation of the site & soil structure.

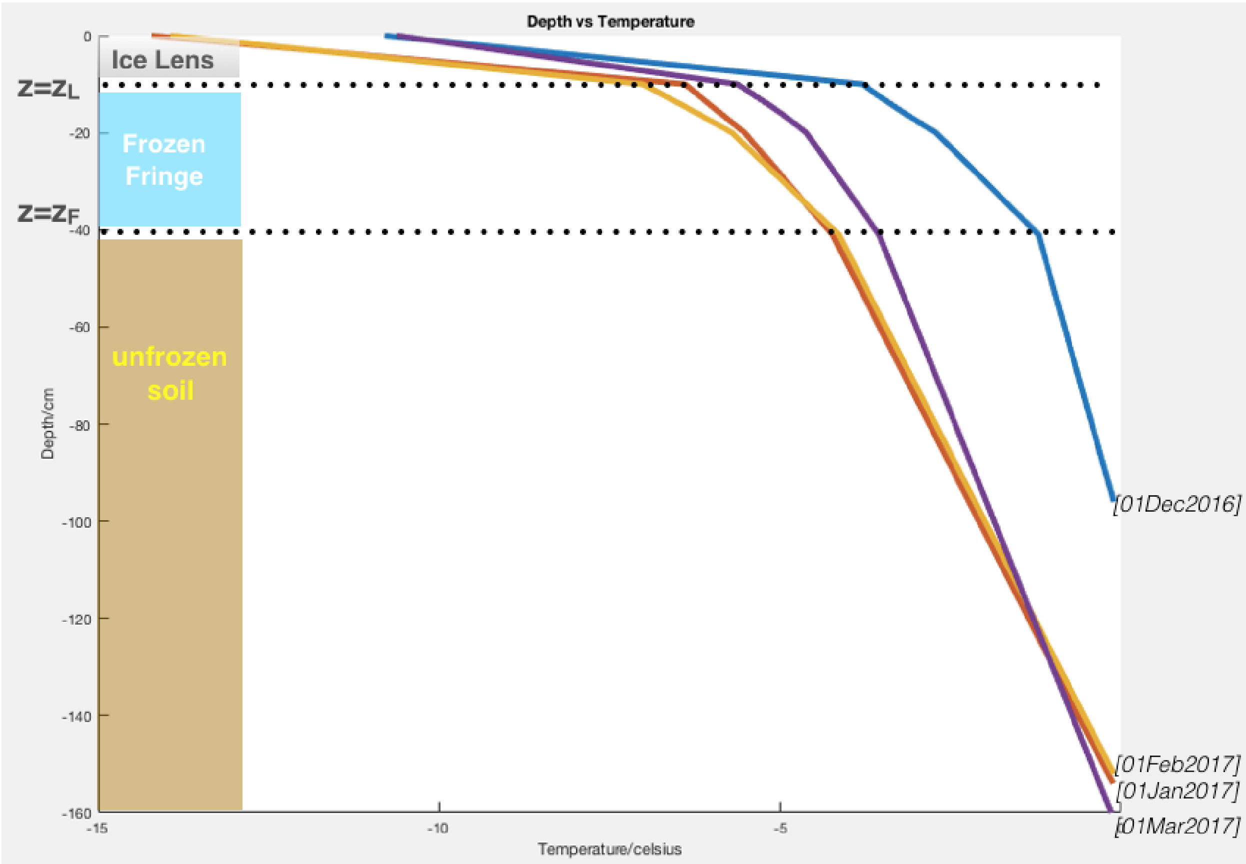

Figure 27. Temperature Profile at the Meadow site for the first of the months December 2016 to March 2017. The temperature is below the melting temperature for ice and gets warmer at deeper points. The estimate for the depth at which ice lens forms is denoted by $z=z_L$. The frozen fringe forms at $z=z_F$. The graphs match the conditions for frost heave.

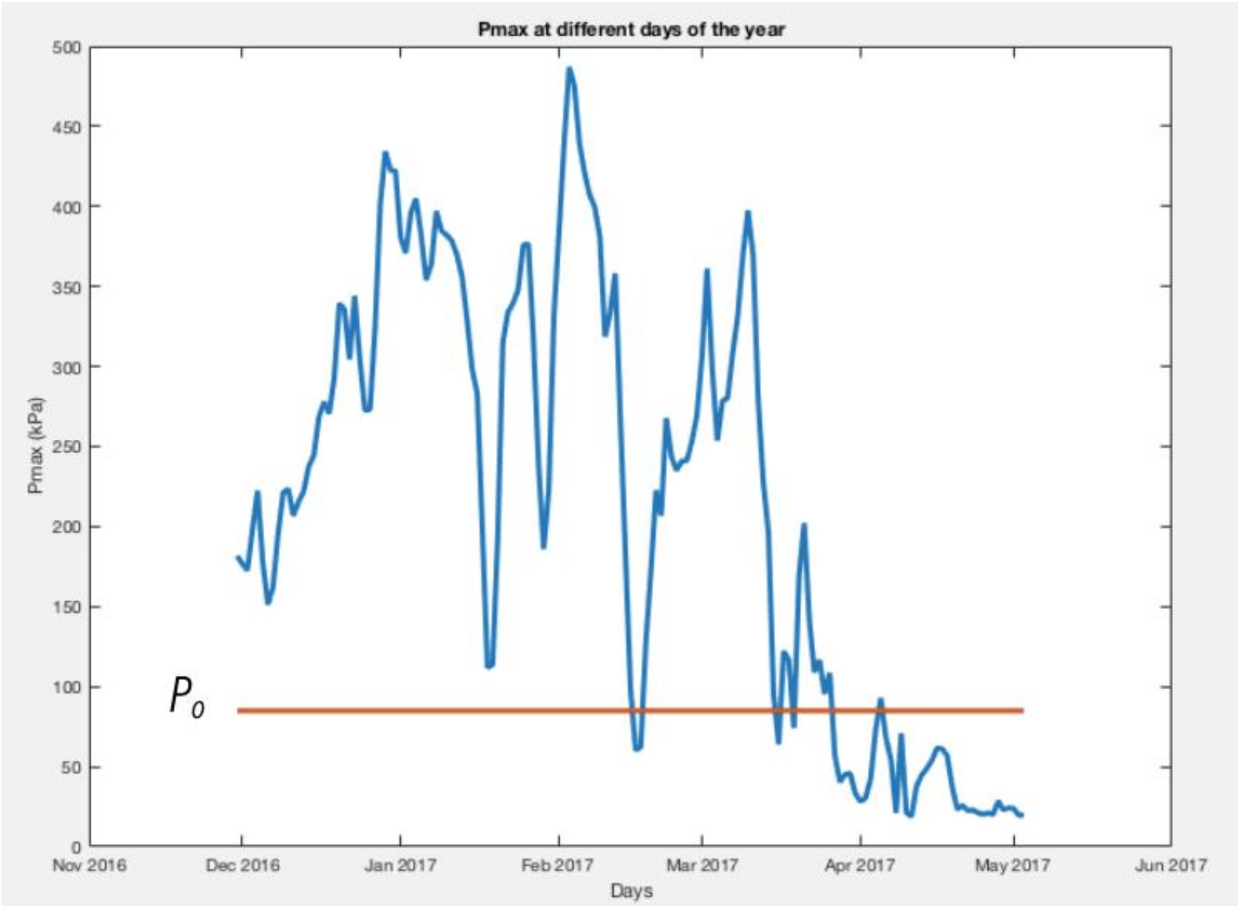

Figure 28. The graph of maximum intermolecular pressure measured during the period of 30 of November 2016 to 9 of May 2017 at the Meadow site. The red line indicates the constant downward pressure on the surface based primarily on the elevation of the site & soil structure.

DISCUSSION

The treeless ridge (meadow) in the study area is determined by the structural geology, lithology, weather (precipitation and above ground and belowground temperature), and groundwater. All of these contribute through the frost heave process (Rempel 2007) to prevent survival of trees. Some of these factors cannot easily change; structural geology is one example, while others such as precipitation and temperature change on time spans in the order of hundreds to thousands of years.

The NW-SE strike of the Dyson fault determines how the westerly wind over the Main and Front Ranges of the Canadian Rocky Mountains strikes perpendicular to the ridgeline (Figure 1) and thus effects how snow is deposited. The winter winds generally blowing from SW/W to NE/E (dominant wind 270□ and 180□) with speeds as high as 50 km/h (Figure 6). The SW site with its covering of trees and increased roughness of the flow of air over the forest accommodates a deeper snow cover throughout the winter. The ridge's (meadow) treeless condition leads to the transport of winter snow from the meadow site into the NE site. The reason is the transition from trees to the meadow causes increased turbulence as air transition from the SW forest to meadow, increasing shear velocity, the snow flux and snow transport (see Appendix 2 on wind flow model, Figure 30S). Also, as the ridge slope increases near the top the airflow increases in velocity, caused by the compression of the flowlines (Johnson and Miyanishi 2010; Liston and Elder 2006). Further, on the NE site, a separation bubble of divergent flow is created, decreasing shear velocity and causing transported snow to be deposited.

Seeds from trees in the forested SW site are dispersed at the end of fall and travel primarily toward the direction of the dominant wind into the meadow where they overwinter (Alexander and Shepperd 1984; Greene & Johnson 1998, 2000; 1989, 1995). Having received the required cold treatment in winter (Franklin 1974, Johnson and Fryer 1996) the next spring they receive sufficient moisture to germinate (Figure 13) and grow to a length to root in the regolith (Appendix 3, Figure 31S)

The effects of lithology are primarily by its influence on infiltration rates, and, hence, regolith's water content. The lithology varies a little between the Meadow and the NE sites where there is steep dipping sandstone and highly weathered shale producing a deeply weather regolith and very high infiltration rates in the Meadow (Table 1). While the SW site contains sandstone and conglomerates with somewhat reduced infiltration rates compared to the Meadow.

The lithology and structural geology of the detached fold allows the surface stratum in the NE site to contribute snow melt water to the meadow in the spring causing a short spring increase in water table (Figure 7).This is confirmed by the springs that drain into first order steams from the meadow sites (Figure 8) that begin to flow in April and May just as the snow is melting on the NE site and then stop when the snow has melted.

The precipitation from October to April (Figure 9) is as snow. In the forested sites the (NE and SW) snow accumulates to a depth that it prevents regolith from freezing (Figure 7). In the meadow the ground is frozen (Figure 7) as a result of lack or very little snow. This is confirmed by observation and satellite images. In April regolith moisture starts to increase as temperature increases at all sites and snow melts in the two forested sites. The summer moisture at the meadow and NE sites is lower than SW site. The meadow's lower regolith moisture is due to little or no snow to melt and high infiltration (Figure 7 & Table 1). The NE is not due to lack of snow but drainage to the meadow. Thus, we conclude in the spring snow melting period, on the meadow the increase in water table (level of saturated regolith) and its decease in summer is the result of a frozen sub-regolith layer because of no snow cover in the winter and subsurface movement of water from the NE site to the Meadow through the similar strata.

The spring water potential is adequate for seed germination and growth but summer for shallow rooted seedling maybe stressful (Figure 13). For plants to be in hydraulic failure, the soil water potential must be as low as the water potential at stomatal closure (Jarvis 1976; Manzoni, Stefano; Katul, Gabriel; Porporato 2014; Martinez-Vilalta *et al.* 2014; Beerling 2015). The matric water potential of the meadow never goes above -0.5 MPa during the growing season (Figure 10) much lower than the traditional wilting point of -1.5 MPa (Davidson, Belk & Boone 1998; Veihmeyer and Hendrickson 1928). The water potential leading to 50% stomata closure in conifers is between -1 MPa and -3 MPa (Manzoni, Stefano; Katul, Gabriel; Porporato 2014). The value when stomata start closing for *Picea Engelmannii*, *Abies lasiocarpa* and *Pinus contorta* is -1.2 MPa before sunrise and -1.4 MPa at mid-day (conifer trees stress categories classification: pmsinstruments.com). The leaf water potential for 8 trees in our sites were measured with a Scholander Pressure Bomb (Appendix 1, Table 6S) in the summer (June 23, 2016) every hour from 4am to 2pm had the lowest water potential of -0.53 MPa. Consequently, the water potential is never low enough to significantly reduce the growing rate of seedlings. The germination process is mostly complete by the end of summer. On the other hand, newly germinated seedlings are small with shallow rooting depths (see Appendix 3, 31S) and are easily uprooted in winter.

Now we will look at the meadow frost heave process. At the NE and SW sites, located in the forest, snow accumulation of ~1m provides insulation. At these sites, the temperature does not increase linearly with depth reaching 0°C. Instead the temperature fluctuates, following the soil moisture profile (Figures 16-20) therefore, P_{max} will never become greater than the overburden pressure (P_0). Ice lens cannot form at higher overburden pressures and relatively warm surface temperatures; water freezes in the pore space without any additional deformation (Rempel 2007). Lens formation is therefore a function of temperature, overburden pressure (Equation 9), known material properties and pore space characteristics (Equation 8).

For frost heave to take place three distinct regions must exist underground as described in the results. The frozen ice-lenses that forms the top layer is constantly pushed upward, causing the actual heaving of the ground above it, by the flow of liquid water through the frozen fringe, the second layer underneath the ice lens. Therefore, water in liquid state must reside underneath the frozen fringe, constituting the third layer, in order to provide the upward flow of water that feeds the ice lens and, at the same time, generates pressure to the ice lens by dynamically interacting with the ice-particles inside the frozen fringe. For the water in liquid state to exist, the temperature increases from the ice lens through the frozen fringe, all the way to the water freezing/melting temperature leading to the region of liquid water. In the NE & SW sites, the conditions for the formation of the three layers are not satisfied. The daily temperature profile obtained via measurements and modeling at different depths throughout the year clearly demonstrates that the temperature does not increase, and the freezing point is not reached, so that water cannot exist in liquid form.

In the fall and winter, snow replaces rain. Snow is blown off the ridgeline. The temperatures close to the surface becomes very low, while deeper down in the regolith, the temperature remains higher. This high temperature causes a heat gradient toward the regolith surface, combined with the sufficient regolith moisture, relatively low overburden pressure (close to the surface and no added snow pressure) and frost susceptible regolith (high silt content). All of these factors lead to frequent frost-heaving that lasts from November to March (Figure 26 & 28). Thus, frost-heaving depends on the environmental factors: overburden pressure and the characteristics of soil (Rempel 2010). These conditions allow a lens to form parallel to the ground surface at depths where temperature falls below melting temperature (~0°C), also known as the "frozen fringe" underneath it. The frozen fringe is a mixture of ice, liquid water, and mineral particles. Available water is drawn toward the lens at a rate described by Darcy's law, since fluid moves toward cooler temperatures (lower pressure). The movement of water results in applying pressure on the soil and causes the observable deformation of the heave (Rempel 2007). Consequently, the length of the winter period when frost heave can take place was determined empirically, and with modeling. The empirical evidence of seedling survival demonstrating that seedlings have little chance of not being uprooted, are consistent with the frost heave period thus derived.

Besides these empirical measurements of surface movement and physical variables are consistent with the models of frost heave, there are periglacial landforms in the meadow: active parallel stone stripes and a series of non-active solifluction lobes on a nearby meadow on a much steeper slope (Figure 29). Stone stripes are one of many forms of patterned ground that evolve overtime from other forms of patterned ground such as circles and polygons. Models have shown that frost heaving causes the formation of these shapes (Kessler & Werner 2003). The shape that forms depends on the frequency of larger rocks found amid finer soil, together with the frequency of freeze-thaw cycles. Stone stripes usually form when the slope is between 2° and 9° (Ballantyne 2001; King 1971). At the soil surface, fine porous soil has more ability to retain water.

Therefore, it expands and contracts as freezing, and thawing takes place, and where there are high proportions of larger rocks, they are pushed into clusters and stripes. When soil freezes, Ice lenses form that move the soil toward soil-rich areas and rocks toward rock-rich areas. Stones are then transported along their axes and squeezed, as thawing expands the soil. This diurnal or annual expansion and contraction of soil causes the self-organization of the regolith at the surface (Ballantyne 2001, Jonasson and Callaghan 1992, Kessler & Werner 2003, King 1971). At Jumping Pound Ridge there is an average of ~1.7 cm regolith displacement per year (Figure 15). Therefore, the stripes are actively developing under the present periglacial regime and are not merely a remnant from the Cavell advance. Patterned ground formation at Jumping Pound is aided by two conditions: the texture of the regolith, i.e. a mixture of clasts in a milieu of frost-susceptible soil, and the existence of moderate slopes (Tables 2, 3 & 4). One question that arises here is that even though there have never been trees in the ridgeline of Jumping Pound, will this be the case for the future as well?

One advantage of approaching a question by finding out the mechanism behind it is that we can vary the results by changing different parameters to see if the outcome changes. This approach allows us to find out the governing parameters and enables us to use our model in other locations with similar properties.

For trees to be able to grow in Jumping Pound ridge regolith movement needs to stop. For this to occur the condition in Equation (8 and/or 9) must not be violated. Equation (8) will hold in almost all mountain landscapes since average pore radius of any combination of clay, sand and silt will always be much less than the right hand side of the equation. In the right side of Equation (8) surface energy of the solid-liquid interface γ_{sl} is a constant, so we are left with porosity φ and the overburden pressure P_0. Changing either or both parameters all the way to their extremes will not change the outcome. The only way that the conditions in this equation will be violated is if Equation (8) were applied to a landscape that is predominantly comprised of gravel.

In Equation (9), there are two parameters that can change the outcome. Temperature gradient G and the fraction of pore volume that is filled with ice S_s. G is calculated based on the change of temperature with depth and latent heat of fusion (Equation 10). Changing the temperature gradient can radically change the outcome as can also be seen from the results obtained from the NE & SW sites where very low temperature gradients caused P_{max} to remain below P_0. Percentage of ice in pore volume S_s is estimated using gravimetric water content, and parameters A and B, which are constants based on soil type. As long as the water content is not close to zero ($w_{tot} << 1\%$), the value of S_s does not vary greatly.

Therefore, the main driver of the process of frost-heave is the extent of change of temperature with depth. The greater the gradient, the larger the P_{max} , which means more heaving. Changing the value of G by one decimal place will results in an increase in P_{max} of two orders of magnitude. Hence, the main driver of frost-heave is soil temperature gradient: the steeper the gradient, the greater the magnitude of frost-heaving. This means that the surface must get sufficiently cold to create a large temperature gradient with depth. A sizable temperature gradient is created only when the surface lacks the insulation of snow. In turn, the absence of snow is made possible by the high velocity winds and by wind patterns that are created by the shape of the ridgeline.

Figure 29. Upper right) Stone stripes on the Meadow from far away, showing a parallel trend. Upper left) Stone stripes on the Meadow, close-up. Bottom) Solifluction lobe on the nearby steeper meadow.

REFERENCES

Alexander, R. R. & Shepperd, W. D. (1984). Silvical Characteristics of Engelmann Spruce. *Rocky Mountain Research Station Publications.* USDA Forest Service, General Technical Report RM-114.

Andersland, O. B. & Ladanyi, B. (2004) Frozen Ground Engineering. Second edition. ASCE & Wiley. Hoboken, NJ.

ASHRAE Handbook of Fundamentals. (1991) Heating, ventilating, and air-conditioning applications (SI ed.). American Society of Heating, Refrigerating and Air Conditioning Engineers Atlanta.

Ballantyne, C.K. (2001) The sorted stone stripes of Tingo Hill. *Scottish Geographical Journal*, **117**, 313–324.

Beerling, D.J. (2015) Gas valves, forests and global change: a commentary on Jarvis (1976) "The interpretation of the variations in leaf water potential and stomatal conductance found in canopies in the field." *Philosophical Transactions of the Royal Society B: Biological Sciences*, **370**, 20140311–20140311.

Chanzy, A., Gauda, JC. & Marloie, O. (2012) Correcting the temperature influence on soil capacitance sensors using diurnal temperature and water content cycles. *Sensors*, **12,** 9773-9790.

Charron, I. & Johnson, E.A. (2006) The importance of fires and floods on tree ages along mountainous gravel-bed streams. *Ecological Applications*, **16**, 1757–1770.

Collins, B.M., Everett, R.G. & Stephens, S.L. (2011) Impacts of fire exclusion and recent managed fire on forest structure in old growth Sierra Nevada mixed-conifer forests. *Ecosphere*, **2**.

Dash, J.G., Rempel, A.W. & Wettlaufer, J.S. (2006) The physics of premelted ice and its geophysical consequences. *Reviews of Modern Physics*, **78**, 695–741.

Davidson, E.A., Belk, E. & Boone, R.D. (1998) Soil water content and temperature as independent or confounded factors controlling soil respiration in a temperate mixed hardwood forest. *Global Change Biology*, **4**, 217–227.

Elrick, D.E. & Reynolds, W.D. (1992) Methods for Analyzing Constant-Head Well Permeameter Data. *Soil Science Society of America Journal,* **56**, 320.

Everett, D.H. (1961) The thermodynamics of frost damage to porous solids. *Transactions Faraday Society*, **57**, 1541–1551.

Florides, G. A. & Kalogirou, S. A. (2005) Annual ground temperature measurements at various depths. *ResearchGate*, 2014, 1-6.

Franklin, D. A. (1974) Beech (nothofagus) Silviculture in the South Island. *Proceedings (New Zealand Ecological Society).* **21,** 17-20.

French H. (1996) The Periglacial Environment. Second edition. Addison Wesley longman: Marlow, Essex.

Gadd, B. (2008) Canadian Rockies Geology Road Tours. Corax Press. Alton, Manitoba.

Greene, D.F. & Johnson, E.A. (1989) A Model of Wind Dispersal of Winged or Plumed Seeds *Ecology*, **7**, 339-347.

Greene, D.F. & Johnson, E.A. (1995) Long-distance wind dispersal of tree seeds. *Canadian Journal of Botany*, **73**, 1036-1045.

Greene, D.F. & Johnson, E.A. (1998) Seed mass and early survivorship of tree species in upland clearings and shelterwoods. *Canadian Journal of Forest Research*, **28**, 1307–1316.

Greene, D.F. & Johnson, E.A. (2000) Tree recruitment from burn edges. *Canadian Journal of Forest Research*, **30**, 1264–1274.

Harsch, M.A., Hulme, P.E., McGlone, M.S. & Duncan, R.P. (2009) Are treelines advancing? A global meta-analysis of treeline response to climate warming. *Ecology Letters*, **12**, 1040–1049.

Jarvis, P.G. (1976) The Interpretation of the Variations in Leaf Water Potential and Stomatal Conductance Found in Canopies in the Field. *Philosophical Transactions of the Royal Society B: Biological Sciences*, **273**, 593–610.

Johnson, E. A. and Fryer, G. I. (1996) Why Engelman spruce does not have a persistant seed bank. *Canadian Journal of Forest Research*, **26,** 872-878.

Johnson, E. A. and Miyanishi, K. (2010) Plant disturbance ecology, the process and the response. University of Calgary. Calgary, Alberta, Canada.

Jonasson, S. & Callaghan, T. V. (1992) Root mechanical properties related to disturbed and stressed habitats in the Arctic. *New Phytologist*, **122**, 179–186.

Kessler, M. A. & Werner, W. T. (2003) *Self-Organization of Sorted Patterned Ground*. Science. **299,** 380-383.

King, R. B. (1971) Boulder Polygons and Stripes in the Cairngotm Mountains, Scotland. *Journal of Glaciology.***10,** 375-386.

Korner, C. (1998) A re-assessment of high elevation treeline psoitions and their explanation. *Oecologia*, **115**, 445–459.

Körner, C. & Paulsen, J. (2004) A world-wide study of high altitude treeline temperatures. *Journal of Biogeography*, **31**, 713–732.

Korner, C. and Riedl, S. (2012) Alpine treelines, fucntional ecology of the global high elevation tree limits. Basel, London: Springer.

Kruckeberg, A. R. (2002) Geology and plant life. The ffects of landforms and rock types on plants. University of Washington. Seattle, WA, USA.

Lakshmi, V., Jackson, T. J. & Zehrfuhs, D. (2003) Soil moisture-temperature relationship: results from two filed experiments. *Hydrological processes,* **17,** 3041-3057.

Leonelli, G., Coppola, A., Baroni, C., Salvatore, M.C., Maugeri, M., Brunetti, M. & Pelfini, M. (2016) Multispecies dendroclimatic reconstructions of summer temperature in the European Alps enhanced by trees highly sensitive to temperature. *Climatic Change*, **137**, 275–291.

Liston, G.E. and K. Elder. 2006. A distributed snow-evolution model (SnowModel). American Meteorological Society, **7**, 1259-1276.

Malanson, G.P., Butler, D.R., Cairns, D.M., Welsh, T.E. & Resler, L.M. (2002) Variability in an edaphic indicator in alpine tundra. *Catena*, **49**, 203–215.

Manzoni, Stefano; Katul, Gabriel; Porporato, A. (2014) Water Resources Research. *AGU Publications*, 5170–5183.

Martinez-Vilalta, J., Poyatos, R., Aguade, D., Retana, J. & Mencuccini, M. (2014) A new look at water transport regulation in plants. *New Phytol*, **204**, 105–115.

Matsuoka, N. (1998) Modelling frost creep rates in an alpine environment. *Permafrost and Periglacial Processes*, **9**, 397–409.

Nixon, J.F. (1991) Discrete ice lens theory for frost heave in soils. *Canadian Geotechnical Journal*, **28**, 843–859.

Oelfke, J.G. & Butler, D.R. (1985) Landslides Along the Lewis Overthrust Fault , Glacier National Park , Montana. *The Geographical Bulletin*, **27**, 7–15.

Osborn, G., Stockmal, G. & Haspel, R. (2006) Emergence of the Canadian Rockies and adjacent plains: A comparison of physiography between end-of-Laramide time and the present day. *Geomorphology*, **75**, 450–477.

Pecher, C., Tasser, E. & Tappeiner, U. (2011) Definition of the potential treeline in the European Alps and its benefit for sustainability monitoring. *Ecological Indicators*, **11**, 438–447.

Pérez, F.L. (1998) Conservation of soil moisture by different stone covers on alpine talus slopes (Lassen, California). *Catena*, **33**, 155–177.

Plasse, C. & Payette, S. (2015) Frost hollows of the boreal forest: A spatiotemporal perspective. *Journal of Ecology*, **103**, 669–678.

Press, C. (2017) The Mechanics of Frost Heaving Author (s): Stephen Taber Source□: The Journal of Geology , Vol . 38 , No . 4 (May - Jun ., 1930), pp . 303-317 Published by□: The University of Chicago Press Stable URL□: http://www.jstor.org/stable/30058950 REFERENCES . , **38**, 303–317.

Rempel, a. W. (2007) Formation of ice lenses and frost heave. *Journal of Geophysical Research: Earth Surface*, **112**, 1–17.

Rempel, A.W. (2010) Frost heave. *Journal of Glaciology*, **56**, 1122–1128.

Rempel, A. W. (2012) Hydromechanical Processes in freezing soils. Vadose Zone Journal.

Rempel, A.W., Marshall, J. a. & Roering, J.J. (2016) Modeling relative frost weathering rates at geomorphic scales. *Earth and Planetary Science Letters*, **453**, 87–95.

Rempel, a W., Wettlaufer, J.S. & Worster, M.G. (2001) Interfacial premelting and the thermomolecular force: thermodynamic buoyancy. *Physical review letters*, **87**, 88501.

Rempel, A.W., Wettlaufer, J.S. & Worster, M.G. (2004) Premelting dynamics in a continuum model of frost heave. *Journal of Fluid Mechanics*, **498**, 227–244.

Roberts, B. A. and Proctor, J. (1992). *The ecology of areas with serpentinized rock, a world view.* Dordrecht: Kluwer Academic Publishers.

Schaap, M.G., Leij, F.J. & Van Gencuhten, M.T. (2002) A computer program for estimating soil hydraulic parameters with hierarchical pedotransfer functions. *Journal of Hydrology*, **251**, 163–176.

Shatford J. P. A., Hibbs, D. E. and Puettmann, K. J. (2007) Conifer regeneration after forest fire in the Klamath Siskiyous: How much, How soon? *Journal of Forestry*, **105**, 139-146.

Shaw, A. J., ed. (1989). *Heavy metal tolerance in plants: evolutionary aspects.* Boca raton, Fla.:CRC Press.

Shuttleworth, W.J. (2007) W . James Shuttleworth Putting the ‘ vap ’ into evaporation Putting the ‘ vap ’ into evaporation. *Water*, **11**, 210–244.

Sperry, J.S. (2003) Evolution of Water Transport and Xylem Structure Author (s): John S . Sperry Source□: International Journal of Plant Sciences , Vol . 164 , No . S3 , Evolution of Functional Traits in Plants (May 2003), pp . S115-S127 Published by□: The University of. *International Journal of Plant Sciences*, **164**.

Slatyer R. O. (1967) Plant-Water relationship. Australian National University. Canberra, Australia.

Van Genuchten, M. (1980) A closed-form equation for predicting the hydraulic conductivity of unsaturated soils. *Soil Science Society of America*, **44**, 892-898.

Veblen, T.T., Hadley, K.S., Reid, M.S. & Rebertus, A.J. (1991) The Response of Subalpine Forests to Spruce Beetle Outbreak in Colorado Author (s): Thomas T . Veblen , Keith S . Hadley , Marion S . Reid and Alan J . Rebertus Reviewed work (s): Published by□: Ecological Society of America Stable URL□: http://www.js. *Ecology*, **72**, 213–231.

Veihmeyer F. J. & Hendrickson, A. H. (1928) Soil Moisture at Permanent Wilting of Plants. *Plant Physiology*. **3,** 355–357.

Wettlaufer, J.S. & Worster, M.G. (2006) Premelting Dynamics. *Annual Review of Fluid Mechanics*, **38**, 427–452.

Wooding, R.A. (1968) Steady Infiltration from a Shallow Circular Pond. Water Resources Research, 4, 1259–1273.

Woods, K.D. (2004) Intermediate disturbance in a late-successional disturbance Intermediate forest hardwood hemlock-northern. *Journal of Ecology*, **92**, 464–476.

SUPPLEMENTARY MATERIAL

Appendix 1.

Table 6S. Field Instrument Table

Instrument	**Manufacturer**	**Accuracy**	**Measuring**
TDR theta probes	Delta-T Devices Ltd.	± 0.01 (cm^3/cm^3)	Soil water content
Temperature probes	HOBO	± 1.0%	Soil temprature
Heat flux HFP01	Campbell Scientific	-15% to +5%	Soil heat flux
Net radiometer	Kipp & Zonen NR-Lite	10 µV/W/m^2	Net radiation
Infrared sensor SI-111	apogee Instruments	0.2 ▯C	Surface temperature
Wind sensor	HOBO	Speed ± 1.1 m/s Direction :± 5 degrees	Wind speed & wind direction
Temprature & humidity sensor	HOBO	Temp: +/- 0.21°C RH: +/- 2.5%	Air temperature & humidity
Rain gauge Onset	HOBO	±1.0%	Percipitation
Tensiometer SK20	UMS	±2.0%	Matric potential
Scholander pressure bomb	PMS Instruments	½ of 1.0%	Plant water potential
Pressure transducer WL16	Global Water	±1.0%	Stream water level

Appendix 2. Distributed snow-evolution model

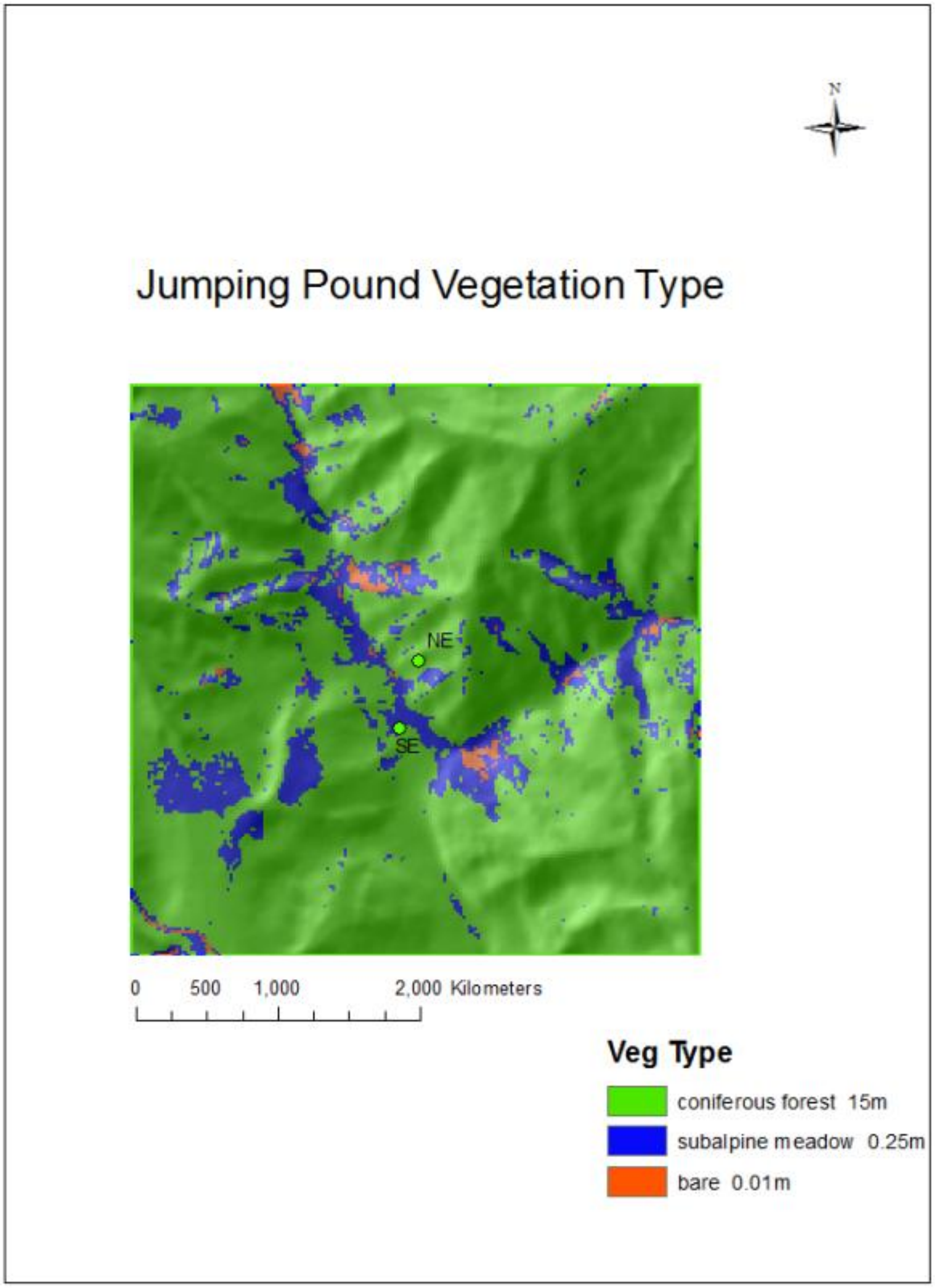

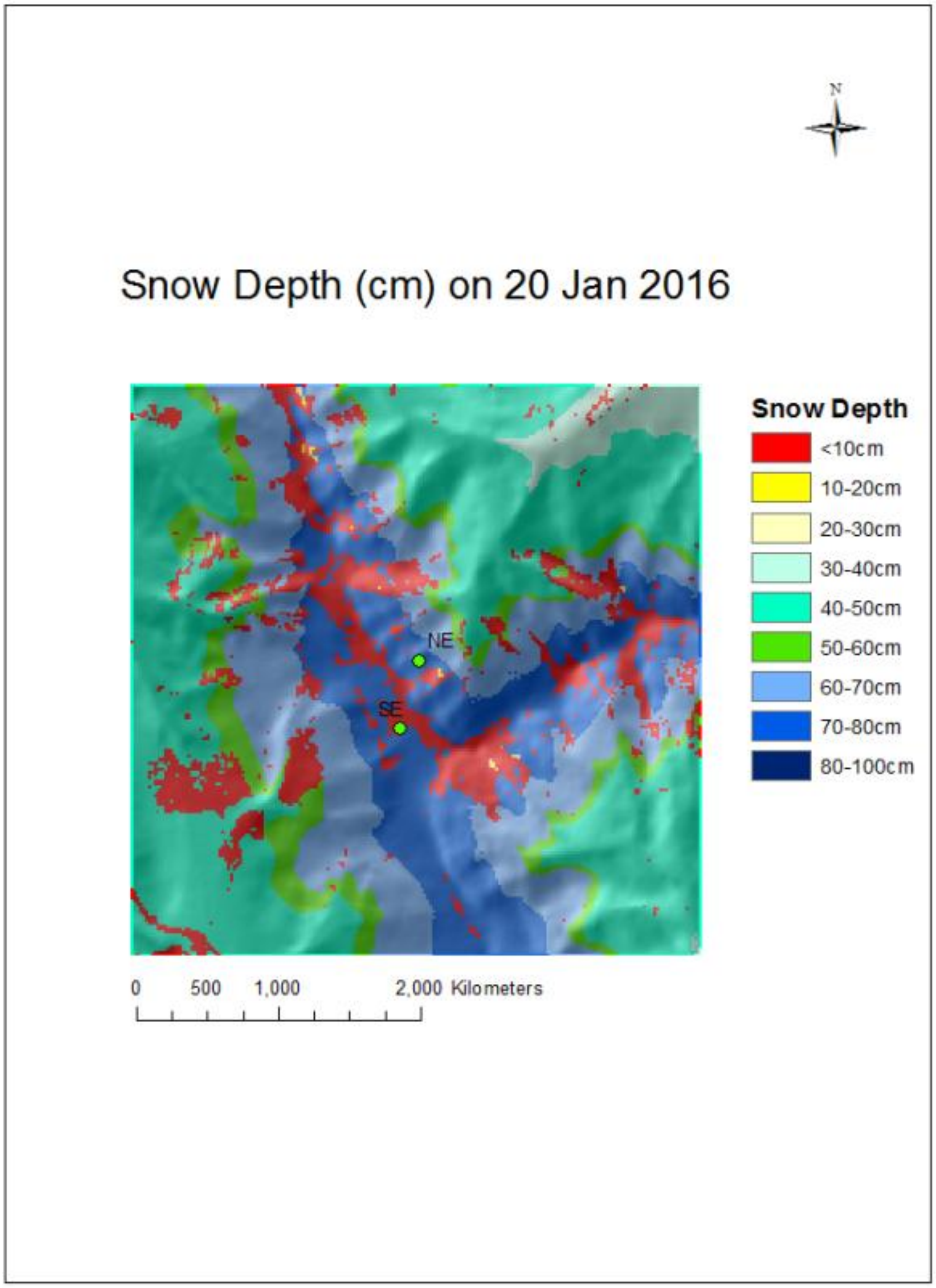

Figure 30S. Figures courtesy of undergraduate independent research by Sara Kroeker (unpublished data). Using Liston and Elder 2006 (SnowModel). First figure shows the vegetation type on our 3 sites, Jumping Pound ridge crest and the 2 forested slopes (NE & SW) and the second figure demonstrates the snow in centimeter in these sites.

Appendix 3. Germinated Seed Sizes

Seeds of the three native tree species (*Abies lasiocarpa*, *Picea Engelmannii and Pinus contorta*) were germinated in the laboratory with the purpose of estimating the size and the rooting depth of newly germinated seedling in the field at the end of summer (Figure 24S) and to complement the "seed planting experiment" performed in field. The establishment success of seedlings can be dependent on root growth during the growing season.

Seeds must grow roots deep enough so that they are not remobilized by the frost heaving of regolith during fall and winter. This experiment shows that after germination takes place, seedlings roots do not grow deep enough by the end of summer to avoid uprooting by frost heave.

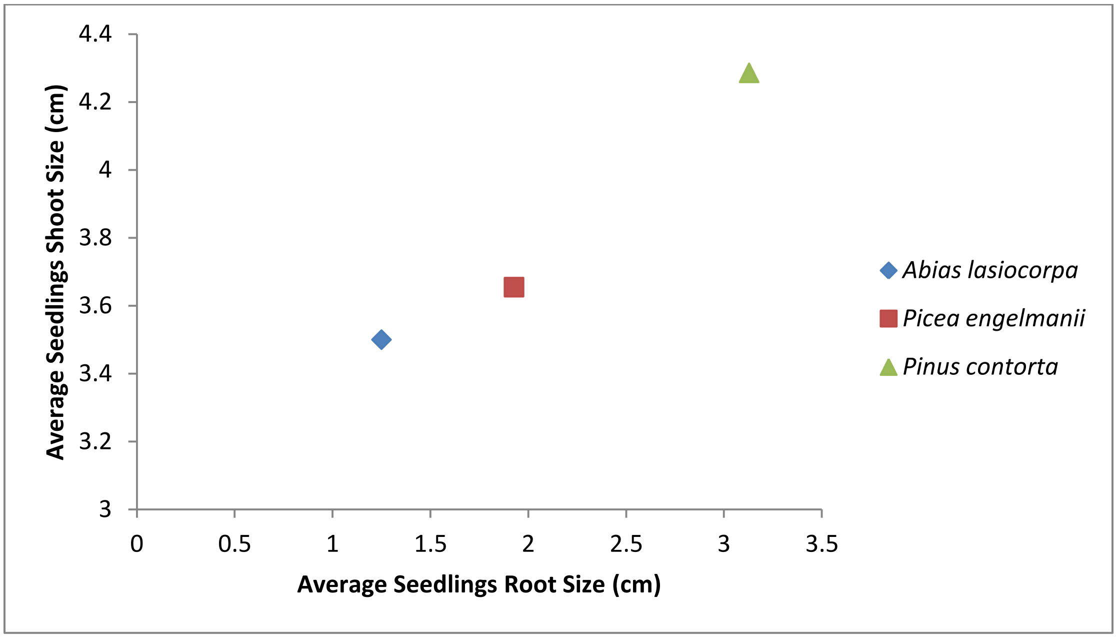

Figure 31S. Average seedling root size vs. average seedling shoot size of *Abies lasiocarpa* (12 replicates), *Picea Engelmannii* (31 replicates) and *Pinus contorta* (24 replicates) for a total of 77 plants measured.